Statistical modelling and direct numerical simulations of decaying stably stratified turbulence. Part 2. Flow anisotropy

Fabien S. Godeferd, Chantal Staquet

J. Fluid Mech. (2003), *vol.* 486, *pp.* 115–159.
DOI: 10.1017/S0022112003004531 Printed in the United Kingdom

Statistical modelling and direct numerical simulations of decaying stably stratified turbulence. Part 2. Large-scale and small-scale anisotropy

By F. S. GODEFERD[1] AND C. STAQUET[2]

[1]LMFA UMR 5509, 69134 Ecully cedex, France
godeferd@mecaflu.ec-lyon.fr

[2]LEGI, BP 53, 38041 Grenoble cedex 9, France

(Received 1 August 2000 and in revised form 9 August 2002)

Stably stratified freely decaying homogeneous turbulence is investigated by means of direct numerical simulations (DNS) and a two-point closure statistical model of the EDQNM type; a careful comparison with laboratory experiments is also made. Several aspects of anisotropy in the flow are studied, both at large and small scales. DNS and EDQNM approaches give very similar results up to the finest indicators of the flow, namely anisotropic spectra of velocity fields. Hence the statistical model predicts the structure of the flow at all scales.

Large-scale anisotropy appears in the Reynolds stress components and in the directional integral length scales. The well-known collapse of vertical turbulent motion, which yields the organization of the flow into quasi-horizontal vertically decorrelated vortex structures, is retrieved and quantified. Thus, the thickness of the vortex structures is shown to be set by their Froude number being of order one, in agreement with a previous dimensional analysis for an inviscid flow. Small-scale anisotropy is quantified from the components of the velocity and temperature gradients, whereby models for the dissipation rate of kinetic energy and available potential energy are discussed. The mixing properties of the flow are also investigated: the counter-gradient heat flux that exists at small scales appears to inhibit mixing when diffusivity is low enough and the Cox number varies linearly with the parameter $\epsilon/\nu N^2$.

All results agree very well with laboratory experiments on stably stratified grid turbulence, though the initial condition of our computations is different from the flow just behind the grid. This suggests a relative independence of decaying stably stratified turbulence of initial conditions.

1. Introduction

A crucial question in homogeneous turbulence subjected to a buoyancy force (and, more generally, to an anisotropic body force) is related to the dynamics of the smallest scales: Are these scales anisotropic or not? On the ability to answer this question depends the parameterization of these scales, an essential issue when, for instance, climate numerical models are considered: Gargett, Osborn & Nasmyth (1984) and Bryan (1987) first showed that predictions of such models are strongly sensitive to slight changes in this parameterization. The dynamics of the smallest scales depend,

of course, upon the Reynolds number of the flow (based upon the Taylor microscale for instance) and upon the parameter measuring the importance, at that same scale, of anisotropic effects relative to nonlinear ones; when buoyancy effects are considered, this parameter is the Froude number *Fr*.

The undersea measurements of Gargett *et al.* (1984), in flows having very large Reynolds but small Froude numbers, showed approximate local isotropy of streamwise velocity gradients (the equivalent mesh Reynolds number is $\simeq 4 \times 10^6$, i.e. at least a hundred times larger than that of typical grid turbulence experiments, while *Fr* varies within the range $[10^{-2}, 5 \times 10^{-2}]$). On the other hand, laboratory experiments of Thoroddsen & Van Atta (1992), whose flow parameters are those of the oceanic thermocline, showed a strong anisotropy when strain rates were compared. The subsequent experimental work of Thoroddsen & Van Atta (1996), on density gradients and scalar dissipation in stably stratified turbulence, showed that these gradients also present a strong anisotropy, and thus that scalar dissipation modelling should be modified accordingly, with respect to the usual isotropic estimates. Models of kinetic energy dissipation have been compared in respect of the anisotropy of velocity gradients by e.g. Yamazaki & Osborn (1990, 1993*a*, *b*), using *in situ* measurements, and by Thoroddsen & Van Atta (1992) and Fincham, Maxworthy & Spedding (1996), using laboratory experiments. In the latter work, stably stratified grid turbulence is studied experimentally using digitized particle image velocimetry and, during the very late stage of the flow, the most important contribution to energy dissipation was identified as coming from the vertical gradient of the horizontal velocity. In the case of sheared stably stratified turbulence, Piccirillo & Van Atta (1997) obtained equivalent results on small-scale anisotropy through measurements of velocity gradients, with an additional effect of the gradient Richardson number; their results demonstrate a significant role of shear in the small-scale structure of the experimental flow however.

In most of these works, large-scale anisotropy is characterized by the ratio w/u of vertical to horizontal r.m.s. velocity components. Values smaller than 1 indicate the dominance of horizontal motion in these flows, and this was also found in channel experiments by Yoon & Warhaft (1990) and Lienhard & Van Atta (1990). Such a large-scale anisotropy has also been observed in numerical work, using direct numerical simulations (DNS) of homogeneous stably stratified turbulence by Riley, Metcalfe & Weissman (1981) and Metais & Herring (1989). The Reynolds number of the simulated flows was relatively low however, due to the coarse numerical resolution. These authors noted an organization of the flow into vertically decorrelated horizontal layers, as a result of a collapse process of the vertical scales (e.g. Riley *et al.* 1981). This collapsed state implies that the two horizontal components of the velocity contribute most to the kinetic energy, but a strong variability of the velocity field remains in all three directions of space. Such a flow organization was later confirmed and studied by numerous authors. For instance, Fincham *et al.* (1996) proposed a simplified way of connecting the vortex lines between vortices contained in adjacent layers. A qualitatively similar structure may also explain the measurements obtained by Sidi (1995) in the stratosphere. The mechanism underlying this flow organization has been investigated theoretically by Godeferd & Cambon (1994) using the EDQNM_2 statistical model (specified below). These authors analysed the triadic interactions between the gravity waves and the horizontal non-propagating (vortex) mode and found that the energy transfer that drains energy from the vertical to the horizontal motion is mainly effected by interactions between three vortex modes. This result is also reproduced by Caillol & Zeitlin (2000) using weak turbulence theory. Dimensional

analysis has also been used to model the quasi-horizontal motions (Riley *et al.* 1981; Lilly 1983; Billant & Chomaz 2001).

Our goal in the following is to study the anisotropy of the flow. By anisotropy, we mean the change in the properties of the flow, whether statistics or deterministic, as a function of the direction of the fluid motions. The flow being statistically axisymmetric about the vertical direction, a feature stemming from the vertical direction of the buoyancy force, only two directions of dependence for the one-point statistical quantities presented will be retained: horizontal and vertical. High-resolution DNS are analysed and an eddy-damped quasi-normal Markovian (EDQNM) type statistical model is compared with the results of the simulations. The model was adapted by Cambon (1989) to stably stratified and rotating turbulent flows and is referred to as the EDQNM_2 model in the following. Its predictions have been shown in Part 1 of this work (Staquet & Godeferd 1998) to be in excellent agreement with those of the simulations, from comparisons of both large-scale and small-scale statistical quantities for flows with different values of Reynolds and Froude numbers.

In the present paper, we shall provide a quantitative description of the large-scale structure of stably stratified freely decaying turbulence, by investigating directional integral length scales that help quantify the structure of the layering of the flow. Our study also includes different indicators of small-scale anisotropy in physical and spectral space, namely velocity and temperature gradients and the spectral distribution of energy. A wave/vortex decomposition, based on the general decomposition of a velocity field proposed by Craya (1958) and used by Herring (1974) and several other authors (e.g. Riley *et al.* 1981; Herring & Metais 1989; Siegel & Domaradzki 1994) will be extensively employed. The analysis of the anisotropy of the velocity gradients will allow us to investigate different models proposed in the literature to compute the dissipation rate of kinetic energy (see references above) and to infer a simpler expression, valid for the present simulations, based upon two gradients only. As well, a simple expression for the dissipation rate of potential energy will be proposed. We shall also address the mixing properties of the flow.

The organization of the paper is as follows. Section 2 recalls the equations for stably stratified homogeneous turbulent incompressible fluids, including a brief description of the wave/vortex decomposition (details are given in Appendix A). The two-point spectral equations are written in this framework, as a starting point for deriving the EDQNM_2 model (with comments in Appendix B). The DNS method and the initial conditions are described in § 3. After characterizing anisotropy in § 4, we discuss results on large-scale (§ 5) and small-scale anisotropy (§ 6). The analysis of mixing is reported in § 7. The finest two-point statistical description of axisymmetric turbulence, namely angular-dependent spectra, are given in § 8, and concluding remarks are collected in § 9.

2. Equations for stably stratified homogeneous turbulence

2.1. *Basic equations*

We deal with stably stratified homogeneous and incompressible turbulence, and we can describe the behaviour of the flow using the Navier–Stokes equations within the Boussinesq approximation (Boussinesq 1901). The equations are written in terms of the fluctuating temperature $T(\boldsymbol{x}, t)$ about a mean temperature of constant uniform vertical gradient $\mathscr{G}$, with $\mathscr{G} > 0$ indicating a stabilizing effect of the stratification upon

the fluid flow. The system of equations in physical space is

$$\left.\begin{aligned}\left(\frac{\partial}{\partial t}+u_j\frac{\partial}{\partial x_j}-\nu\nabla^2\right)u_i+\frac{\partial p}{\partial x_i}&=T\delta_{i3},\\ \left(\frac{\partial}{\partial t}+u_j\frac{\partial}{\partial x_j}-\nu\nabla^2\right)T&=-N^2u_3,\\ \frac{\partial u_i}{\partial x_i}&=0,\end{aligned}\right\} \tag{2.1}$$

where T has been scaled as an acceleration, using the factor βg, where β is the thermal expansion coefficient and g the acceleration due to gravity; x (or subscript 1) and y (subscript 2) are the horizontal directions, and z (subscript 3) is the vertical one. The respective components of the fluctuating velocity will also be denoted u, v and w. The last equation states the incompressibility of the fluctuating velocity field $\boldsymbol{u}(\boldsymbol{x},t)$. The temperature diffusivity κ is here assumed to be equal to the kinematic viscosity ν in the temperature equation, therefore yielding a unit Prandtl number. The solution of the linearized system (2.1) is a combination of three eigenmodes, two of which are internal gravity waves (due to the buoyancy force in the vertical momentum equation). The corresponding linear time scale is $1/N$, where $N=(\beta\mathscr{G}g)^{1/2}$ is the Brunt–Väisälä frequency and $T_{BV}=2\pi/N$ is the corresponding period. The temporal frequencies associated with each of these two propagating modes are

$$\omega^{\pm}=\pm N\sin\theta, \tag{2.2}$$

where θ is the angle of the wavevector to the vertical. The third eigenmode represents the part of the velocity with vertical vorticity, secular in the linear limit since it does not interact with the two wave modes, and therefore corresponds to a zero time frequency $\omega^0=0$.

Using the homogeneity hypothesis, all quantities are Fourier transformed, leading to equations for the Fourier components $\hat{\boldsymbol{u}}(\boldsymbol{k},t)$ of the fluctuating velocity $\boldsymbol{u}$, and $\hat{T}(\boldsymbol{k},t)$ for the temperature T. The spectral space variable is the wavevector $\boldsymbol{k}$. The continuity equation in spectral space is $\boldsymbol{k}\cdot\hat{\boldsymbol{u}}=0$, so that the velocity vector in spectral space is orthogonal to the wavevector, and the pressure gradient term may be suppressed from the equations. The remaining two equations for the Fourier coefficients become

$$\left.\begin{aligned}\left(\frac{\partial}{\partial t}+\nu k^2\right)\hat{u}_i(\boldsymbol{k})-P_{i3}(\boldsymbol{k},t)g\beta\hat{T}(\boldsymbol{k},t)&=-\mathrm{i}k_lP_{in}(\boldsymbol{k})\int_{\boldsymbol{k}+\boldsymbol{p}+\boldsymbol{q}=\boldsymbol{0}}\hat{\boldsymbol{u}}_n(\boldsymbol{p},t)\hat{\boldsymbol{u}}_l(\boldsymbol{q},t)\,\mathrm{d}^3\boldsymbol{p},\\ \left(\frac{\partial}{\partial t}+\nu k^2\right)\hat{T}(\boldsymbol{k})-\mathscr{G}\hat{u}_3(\boldsymbol{k},t)&=-\mathrm{i}k_l\int_{\boldsymbol{k}+\boldsymbol{p}+\boldsymbol{q}=\boldsymbol{0}}\hat{\boldsymbol{u}}_l(\boldsymbol{p},t)\hat{T}(\boldsymbol{q},t)\,\mathrm{d}^3\boldsymbol{p}\end{aligned}\right\} \tag{2.3}$$

where $P_{ij}=\delta_{ij}-k_ik_j/k^2$ is the projector onto the plane orthogonal to $\boldsymbol{k}$, and δ_{ij} is the Kronecker tensor. We also use $\mathrm{i}^2=-1$. The relevant non-dimensional parameters in these equations are the Reynolds number $Re=UL/\nu$ and the Froude number $Fr=U/NL$, where U and L are estimates of velocity and length scales (to be specified later).

2.2. *Two-point spectral equations in the wave/vortex decomposition*

In an attempt to identify the waves in the flow, and separate their dynamics from that of the turbulent motion (see Riley & Lelong 2000 for a review), we shall decompose the velocity field into the orthogonal frame of eigenmodes mentioned above, with corresponding unit vectors $\boldsymbol{e}^i$, which is also referred to as the

Craya–Herring frame. This may be stated equivalently in physical or spectral space as detailed in Appendix A. In spectral space, the velocity field consists of an oscillating mode $\hat{\phi}^2$ related to the internal waves, and a vertical vortex mode $\hat{\phi}^1$. In order to unify the notation, the fluctuating temperature is rewritten as $\hat{\phi}^3 = (\mathrm{i}/N)\hat{T}$. This specific scaling permits to obtain in a single way all the associated energies in the flow, by integrating two-point correlations of the $\hat{\phi}^i$: the vortex energy from $\hat{\phi}^1$, the kinetic wave energy from $\hat{\phi}^2$, and the potential energy from $\hat{\phi}^3$, as explained hereafter.

The spectrum $\hat{V}_{ij}$ of second-order correlations of the fluctuating velocity–temperature $\hat{\boldsymbol{v}} = \hat{\phi}^i \boldsymbol{e}^i$ is defined by $\langle \hat{v}_i(\boldsymbol{p}, t)\hat{v}_j(\boldsymbol{k}, t)\rangle = \hat{V}_{ij}(\boldsymbol{k}, t)\delta(\boldsymbol{k} + \boldsymbol{p})$, where $\langle\ \rangle$ denotes an ensemble average. (As a result of the well-known closure problem in the hierarchy of spectral correlation equations, its dynamical equation also contains the spectrum $\hat{V}_{ijl}$ of third-order correlations $\langle \hat{v}_i(\boldsymbol{k}, t)\hat{v}_j(\boldsymbol{p}, t)\hat{v}_l(\boldsymbol{q}, t)\rangle = \hat{V}_{ijl}(\boldsymbol{k}, t)\delta(\boldsymbol{k} + \boldsymbol{p} + \boldsymbol{q})$.) The components of $\hat{V}_{ij}$ are obtained in the Craya–Herring frame by a double dot product with each of the $\boldsymbol{e}^i$ unit vectors, yielding the following Hermitian matrix:

$$\tfrac{1}{2} e_i^u \hat{V}_{ij} e_j^v = \begin{pmatrix} \Phi_1 & 0 & 0 \\ 0 & \Phi_2 & \Psi^* \\ 0 & \Psi & \Phi_3 \end{pmatrix}. \tag{2.4}$$

From the definition of the Craya–Herring modes, Φ_1 is interpretted as the spectrum of kinetic energy contained in the horizontal vortical motion in the flow, Φ_2 as that of the kinetic energy for the wave motion, and Φ_3 the spectrum of the potential energy associated with the waves. $\Psi = \langle \hat{\phi}^{2*}\hat{\phi}^3\rangle/2$ is the velocity/temperature correlation spectrum, whose integration in the vertical direction leads to the vertical heat flux:

$$\tfrac{1}{2}\langle u_3 T\rangle = -N \int \Psi_R(\boldsymbol{k}) \sin\theta_k \mathrm{d}^3\boldsymbol{k}. \tag{2.5}$$

The subscript R stands for real part. Note how the one-point quantity (2.5) is obtained by means of an integration of Ψ_R over wavevector space. Other one-point statistical quantities (such as the total energies) are computed in an equivalent manner, so that the functional θ_k-dependence of the spectra plays a major role in the integration, whence a need to investigate thoroughly both the $|\boldsymbol{k}|$ and θ_k dependence of the spectra.

The system of exact equations for these spectra stems from the spectral equations (2.3) (equation (A 4) being an intermediate step) and from definition (2.4) and is expressed as

$$\left(\frac{\partial}{\partial t} + 2\nu k^2\right) \Phi_1(\boldsymbol{k}, t) = T^1(\boldsymbol{k}, t), \tag{2.6}$$

$$\left(\frac{\partial}{\partial t} + 2\nu k^2\right) \Phi_2(\boldsymbol{k}, t) + N \sin\theta_k \Psi_R(\boldsymbol{k}, t) = T^2(\boldsymbol{k}, t), \tag{2.7}$$

$$\left(\frac{\partial}{\partial t} + 2\nu k^2\right) \Phi_3(\boldsymbol{k}, t) - N \sin\theta_k \Psi_R(\boldsymbol{k}, t) = T^3(\boldsymbol{k}, t), \tag{2.8}$$

$$\left(\frac{\partial}{\partial t} + 2\nu k^2\right) \Psi_R(\boldsymbol{k}, t) - 2N \sin\theta_k [\Phi_2(\boldsymbol{k}, t) - \Phi_3(\boldsymbol{k}, t)] = T^{\Psi_R}(\boldsymbol{k}, t), \tag{2.9}$$

$$\left(\frac{\partial}{\partial t} + 2\nu k^2\right) \Psi_I(\boldsymbol{k}, t) = T^{\Psi_I}(\boldsymbol{k}, t). \tag{2.10}$$

These equations may be written in tensorial form as†

$$\left(\frac{\partial}{\partial t}+2\nu k^2\right)\boldsymbol{Q}(\boldsymbol{k},t)+\boldsymbol{\Lambda}(\boldsymbol{k},t)\boldsymbol{Q}(\boldsymbol{k},t)=\boldsymbol{T}(\boldsymbol{k},t) \tag{2.11}$$

where $\boldsymbol{Q}=(\Phi_1,\Phi_2,\Phi_3,\Psi_R)$, $\boldsymbol{T}=(T^1,T^2,T^3,T^{\Psi_R})$ and the four-dimensional tensor $\Lambda_{ij}=N\sin\theta_k[(\delta_{i4}-\delta_{i3})\delta_{4j}+2(\delta_{3j}-\delta_{2j})\delta_{i4}]$, thus indicating a direct linear coupling between Φ_2 and Φ_3 through the heat flux Ψ_R, proportional to the internal wave frequency $N\sin\theta_k$. The transfer terms $\boldsymbol{T}$ are obtained in the same way as $\boldsymbol{Q}$ by projecting the nonlinear terms in the $\hat{V}_{ij}$ equation onto the Craya–Herring frame.

Equations (2.11) can be rewritten so as to separate the energy in the vortex part Φ_1 and the total energy in the waves $\Phi_2+\Phi_3$, from the oscillating quantity $\Phi_2-\Phi_3+\mathrm{i}\Psi_R$, as follows:

$$\left(\frac{\partial}{\partial t}+2\nu k^2\right)\Phi_1=T^1, \tag{2.12}$$

$$\left(\frac{\partial}{\partial t}+2\nu k^2\right)(\Phi_2+\Phi_3)=T^2+T^3, \tag{2.13}$$

$$\left(\frac{\partial}{\partial t}+2\nu k^2-2\mathrm{i}N\sin\theta_k\right)(\Phi_2-\Phi_3+\mathrm{i}\Psi_R)=T^2-T^3+\mathrm{i}T^{\Psi_R}. \tag{2.14}$$

This formulation parallels that in the covariance spectra of the velocity–temperature field written in the frame of normal modes of the linear operator, and is the one used in the EQDNM$_2$ model. The EQDNM$_2$ model is the closure of the hierarchy of moments appearing in the nonlinear transfer terms T^i. One must keep in mind the fact that our model, although it bears the same name as the classical isotropic EDQNM one, has been totally redesigned so as to be able to treat the anisotropy at the level of two-point correlations in the spectral formulation. Its main features are briefly discussed in Appendix B, and the reader can refer to Part 1 for a more complete description.

Numerical resolution of the system of modelled equations (2.12)–(2.14) is achieved using an Euler advancement scheme with constant time step. The energy spectra coefficients are solved for wavevectors that lie over a numerical grid in spectral space, with spherical-coordinate discretization: 19 polar angles are chosen between $[0,\pi/2]$ (accounting for the mirror symmetry with respect to the $k_z=0$ plane), and wavenumbers k are logarithmically spread starting from $k_{min}=1/n$, such that $1\leqslant k/k_{min}\leqslant 128$, using a domain side of $2\pi n$.

3. Direct numerical simulations

3.1. *Numerical method*

A numerical pseudo-spectral collocation method expressed in Fourier space is used to solve the system of equations (2.1), as has now become classical in fluid mechanics (e.g. Rogallo 1981; Vincent & Meneguzzi 1991). Prior to solution, the system of equations is rewritten using the vector identity

$$(\boldsymbol{u}\cdot\nabla)\,\boldsymbol{u}=\boldsymbol{\omega}\times\boldsymbol{u}+\frac{\nabla|\boldsymbol{u}^2|}{2},$$

where $\boldsymbol{\omega}=\nabla\times\boldsymbol{u}$ is the vorticity. The boundary conditions are periodic in the three

† Equation (2.10) is decoupled from the others provided $\Psi_I=0$ initially, which is the case in the following.

RUN	Resolution	Duration of run (from t_0)	ν	N	Side of numerical domain	Fr_t	Re_λ	$\epsilon/\nu N^2$
A	256^3	$3T_{BV}$	1/400	π	2π	0.38	58	31
B	256^3	$6T_{BV}$	1/400	$\pi/2$	2π	0.76	58	124
R0	256^3	24	1/300	0	4π	–	45	–
R1	256^3	$6T_{BV}$	1/300	$\pi/2$	4π	0.88	45	98
R2	256^3	$6T_{BV}$	1/300	π	4π	0.44	45	24.5
r2	128^3	$6T_{BV}$	1/150	π	4π	0.45	32	14
r3	128^3	$3T_{BV}$	1/150	π	4π	0.45	32	14
r4	128^3	$3T_{BV}$	1/150	$\pi/2$	4π	0.45	32	56

TABLE 1. Sets of parameters for the different runs of direct numerical simulations and of $EDQNM_2$ computations. ν is the kinematic viscosity and N, the Brunt–Väisälä frequency. t_0 is the time at which N is set to a non-zero value in the pre-computation of isotropic homogeneous turbulence. The last three columns provides the value at $t = t_0$ of a turbulent Froude number Fr_t, of the Reynolds number Re_λ, and of the normalized dissipation rate of kinetic energy ϵ. Fr_t and Re_λ are defined in § 3.3.

directions, and the numerical domain is a cubic box of side 2π or 4π, depending on the run (see table 1). The spatial derivatives are treated numerically in Fourier space using the pseudo-spectral technique. The aliasing effect inherent in this technique (e.g. Canuto *et al.* 1988) is avoided in spectral space by a spherical truncation of the Fourier components of the fluctuating velocity field, using a 2/3 de-aliasing rule at every time step. The time scheme is third-order Adams–Bashforth, and the viscous term is integrated exactly using the new variable $\boldsymbol{w}(\boldsymbol{k}) = \boldsymbol{u}(\boldsymbol{k})\exp(\nu k^2 t)$.

3.2. *Spectra computation*

In Part 1, we have presented isotropically accumulated spectra for the velocity–temperature field $\hat{\boldsymbol{v}}$. These are computed by summing all correlation contributions within a given spherical shell in Fourier space. The value of the kinetic energy spectrum $E(k_n)$ at wavenumber k_n is thus obtained as

$$E(k_n) = \sum_{|\boldsymbol{k}|\in I_n} \hat{\boldsymbol{u}}^*(\boldsymbol{k})\cdot\hat{\boldsymbol{u}}(\boldsymbol{k}),$$

where I_n indicates the spherical shell of width Δk around k_n. An original contribution of the present work is to present angular-dependent spectra, computed from DNS, in order to compare their spectral anisotropy with that of the statistical model. Such anisotropic spectra are suitable for quantifying accurately the anisotropy of the flow. In the statistical model, the angular-dependent spectra are the unknowns in the equations, so that their values are obtained at the nodes (k_n,θ_m) of a discretized (k,θ) grid, as the solution of the time-dependent model equations (2.6)–(2.10). Extracting the same quantities from DNS fields requires a large number of grid points, in order to obtain enough sampling for computing the spectra at each (k_n,θ_m) grid point. We shall not use as many discretized angles in DNS as in $EDQNM_2$: we have found that good enough sampling is obtained for no more than $N_\theta = 5$ angular sectors, in a 256^3 DNS, dividing evenly the $[0, \pi/2]$ interval. The spectra are therefore computed in the following way, e.g. for the kinetic energy:

$$E(k_n,\theta_m) = \frac{\pi/2}{2\Delta\theta}\left[\int_{\theta_m-\Delta\theta/2}^{\theta_m+\Delta\theta/2}\cos\theta\,\mathrm{d}\theta\right]^{-1}\sum_{\substack{|\boldsymbol{k}|\in I_n\\ \theta_k\in J_m}}\hat{\boldsymbol{u}}^*(\boldsymbol{k})\cdot\hat{\boldsymbol{u}}(\boldsymbol{k}), \tag{3.1}$$

where J_m is the part of the spherical shell I_n of angular width $\Delta\theta$ about the angle θ_m. Spectra obtained in this way are dimensionally equivalent to those integrated over spherical shells, so that this procedure allows one to compare the angular dependence to the equivalent isotropic spectrum.

3.3. *Initial conditions and parameters*

Our initial conditions differ from those usually used in DNS, and from the flow just behind the grid in experiments on grid turbulence with stable background stratification. In the latter case, the initial potential energy is almost negligible compared to the kinetic energy. Hence, the initial dynamics of the flow are essentially driven by the linear effects of buoyancy, thus generating large oscillations in the fluid motion. Here, rather, we set the initial condition such that $\Phi_1(t_0) = \Phi_2(t_0) = \Phi_3(t_0)$, so that linear terms are exactly cancelled at $t = t_0$, as shown by equation (2.9). This initial condition implies that the potential energy is half the kinetic energy but 1.5 times the vertical kinetic energy at $t = t_0$. This choice is justified in that it constitutes the most severe test case for comparing the EDQNM$_2$ model to the simulation. Indeed, in that case, the early time evolution of turbulence is set by the nonlinear terms, which contain the closure assumption in the EDQNM$_2$ model. Therefore, if a defect of the EDQNM$_2$ model is to appear, it will be largest in that case, and will not be hidden by other phenomena. In addition, in order to achieve initial dynamics that are as physical as possible, the stratified runs are initialized with a velocity field obtained from an isotropic pre-computation (assumed to correspond to times smaller than t_0), which allows triple correlations of the velocity field to reach their fully developed state value. The temperature field at t_0 is randomly distributed, and the velocity/temperature correlations start to build up under the action of the stratification effect which is imposed from this time on.

For comparison with laboratory experiments, we also performed two runs with zero potential energy at $t = t_0$ (referred to as runs r3 and r4 in table 1). We shall see that, apart from an initial transient, the anisotropic state reached after a couple of Brunt–Väisälä periods in the other runs is nearly the same as in the case of zero initial potential energy. The same conclusion will therefore be drawn when comparing with experimental results.

The parameters for the different simulations are shown in table 1. Fr_t and Re_λ respectively are a turbulent Froude number, and the Reynolds number based upon the Taylor length scale λ:

$$Fr_t = L_b/L = \frac{w/N}{u^3/\epsilon}, \qquad Re_\lambda = \frac{u\lambda}{\nu}; \tag{3.2}$$

u and w respectively denote the r.m.s. of the horizontal and vertical velocity components; ϵ is the dissipation rate of total kinetic energy E_k; and $\lambda = \sqrt{10\nu E_k/\epsilon}$. At the end of the computations, the Reynolds number has decreased to about 30; the Froude number is equal to $\simeq$0.15 after one Brunt–Väisälä period and $\simeq$0.02 after 6 Brunt–Väisälä periods.

4. Overall flow dynamics and anisotropy characterization

4.1. *Overall flow dynamics*

The analysis of the energetics of the flow reported in Part 1 has allowed us to extract several key features of the flow. We shall summarize these features here, in order to help understand how anisotropy develops at large and small scales.

One of the well-known effects of the restoring vertical buoyancy force upon an incompressible turbulent fluid is to reduce the kinetic energy of turbulence in the vertical direction. Indeed, potential energy is transferred toward small scales more efficiently than kinetic energy (Ramsden & Holloway 1992; Lesieur 1990; Part 1), while the small Froude number of the largest scales ensures a continuous (reversible) conversion of vertical kinetic energy into potential energy. In our calculations, these properties yield that the flow dynamics during the first half-Brunt–Väisälä period is controlled by the initial condition: because a large amount of potential energy is present initially, the higher transfer rate of potential energy toward small scales leads to a 30% decrease of the vertical kinetic energy, relative to the decrease that would occur if the flow were non-stratified, to make up for the large-scale potential energy loss. The vertical kinetic energy next decays like its isotropic counterpart, but at a lower level, to $1.5T_{BV}$. The flow is marked by a second event at this time, consisting of all scales of motions, up to the smallest, being influenced by buoyancy effects. This means that the Osmidov scale $L_o = (\epsilon/N^3)^{1/2}$, at which buoyancy and inertial effects balance, reaches the Kolmogorov scale $\eta = (\nu^3/\epsilon)^{1/4}$, at which dissipative and inertial effects balance. It can indeed be inferred from figure 13(*a*) of Part 1 that $\epsilon/\nu N^2$, which is equal to $(L_o/\eta)^{4/3}$, reaches a value of 1 at $1.5T_{BV}$. This result is consistent with the smallest ratio of L_o/η being equal to 2 in the laboratory experiments of Lienhard & Van Atta (1990) and the smallest scales following isotropic dynamics during the whole duration of the experiment (note that the time at which $\epsilon/\nu N^2 = 1$ strongly depends upon the Reynolds number of the flow, as found by Huq & Stretch 1995). In our numerical simulations, the heat flux is found to collapse at $1.5T_{BV}$ as well. Note that 'collapse' does not mean 'vanish'; the volume-averaged heat flux is dominated by the largest scales of the flow and is therefore oscillating about zero. What we mean by collapse is a sudden decrease in amplitude, by a factor 10 or so, relative to its maximum value, occurring at about $1.5T_{BV}$. This suggests that the smallest dynamical scales become dominated by the buoyancy force from this time on because they are fed with insufficient energy by the largest scales.

The fact that the buoyancy force dominates the small-scale dynamics from $1.5T_{BV}$ implies that the Froude number of these scales is of order 1 at that time. This also explains why statistical quantities associated with small-scale motion, such as the vertical kinetic energy (figure 11 of Part 1) and the dissipation rate of kinetic energy (figure 13) display a similarity law from $1.5T_{BV}$, when plotted as a function of $(t - t_0)/T_{BV}$ to account for cumulative effects of buoyancy, and when normalized by their instantaneous isotropic counterparts to account for cumulative effects of viscous dissipation.

The horizontal velocity component normalized by its instantaneous isotropic counterpart (figure 12 of Part 1) behaves quasi-independently of N and of the viscosity when plotted as function of $(t - t_0)T_{BV}$, up to $1.5T_{BV}$. More precisely, this quantity remains close to 1 up to $\simeq 0.7T_{BV}$, meaning that the horizontal velocity component decays isotropically and thus remains unaffected by the increased loss (compared to the isotropic case) of vertical kinetic energy during that stage. (The latter result was also observed by Lienhard & Van Atta 1990 in their wind tunnel experiments.) The normalized r.m.s. horizontal velocity next starts to increase, meaning that a reduction of energy transfer to the small scales, with respect to the isotropic case, has been initiated due to buoyancy effects. From $1.5T_{BV}$, the curves start to separate, depending on the values of N and of the viscosity, but still continue to increase. This signals that large-scale quasi-horizontal motions have emerged from turbulence.

4.2. *Anisotropy characterization*

We will refer to 'directional' anisotropy as the dependence of the spectra on the orientation of the wavevector, i.e. the variation when $\boldsymbol{k}$ is rotated from the vertical direction (pole) to the horizontal one (equator), its modulus being kept constant. On the other hand, for a given wavevector, the difference between $\hat{\phi}^1$ and $\hat{\phi}^2$ is the 'polarization' anisotropy. When $\boldsymbol{k}$ is vertical, statistical axisymmetry amounts to $\Phi^1(\boldsymbol{k}) = \Phi^2(\boldsymbol{k})$. This formalism has been extensively used by e.g. Cambon, Mansour & Godeferd (1997), in the case of rotating homogeneous turbulence, by introducing a *directional* anisotropy tensor and a *polarization* anisotropy tensor. We also note that Reynolds & Kassinos (1994) define tensorial quantities which can be computed in physical space, namely the *dimensionality structure* tensor, and the *circulicity* one. Both formalisms are equivalent when describing the flow anisotropy at a higher level than the one-point statistical one.

Though useful in many instances of anisotropic flows, these quantities can be more specifically used in the stably stratified case, as an accurate characterization of the 'collapse' of the turbulent flow to a two-component three-dimensional state.

5. Large-scale anisotropy

5.1. *Velocity components*

The ratio u/w is displayed in figure 1(a) for DNS computations, and in figure 1(b) for the corresponding EDQNM$_2$ results. In DNS, u is the average of the two r.m.s. components u_1 and u_2 (the fluid motion being statistically symmetric about the vertical axis).

Figure 1(a) shows that the ratio is larger than 1 for all $t > t_0$. Thus, the anisotropy at large scales develops from the very beginning of the runs. As just explained, this behaviour is accounted for (during the first Brunt–Väisälä period) by the loss of vertical kinetic energy being stronger than the isotropic loss, because of potential energy conversion, while u remains nearly unaffected by buoyancy effects. The striking feature of the figure is the independence from N and ν up to 1.5 Brunt–Väisälä periods. The existence of this unique dependence can be accounted for by noting that

$$\frac{u}{w} = \frac{u}{u^{N=0}} \, \frac{w^{N=0}}{w} \, \frac{u^{N=0}}{w^{N=0}}, \tag{5.1}$$

where $u^{N=0}$ and $w^{N=0}$ denote the r.m.s. values of the horizontal and vertical components in the corresponding isotropic flow. In the isotropic flow, $u^{N=0}/w^{N=0}$ remains close to $\simeq 1$ over time, since both velocity components decay at the same rate and are equal at the initial time. Also, we noted in § 4.1 that $u/u^{N=0}$ and $w/w^{N=0}$ behave independently of N and ν when plotted as a function of $(t - t_0)/T_{BV}$ up to $1.5T_{BV}$.

From $1.5T_{BV}$, u and w become associated with entirely different anisotropic motion: u mostly comes from large-scale quasi-horizontal motions while w mostly belongs to the three-dimensional internal wave part. If the former motions were two-dimensional, u would be conserved (except for viscous effects), while w must decrease because of nonlinear transfers toward small scales; u actually decays, but less than w (see Part 1) so that the ratio u/w increases. The lowest-viscosity runs A and B behave differently from $1.5T_{BV}$. The ratio u/w remains nearly constant, which implies that u and w decay at the same rate. The lower viscosity of these runs and a possible confinement effect of the largest scales may account for this behaviour. The EDQNM$_2$ model does not reproduce this difference however (figure 1b): u/w eventually reaches a value of

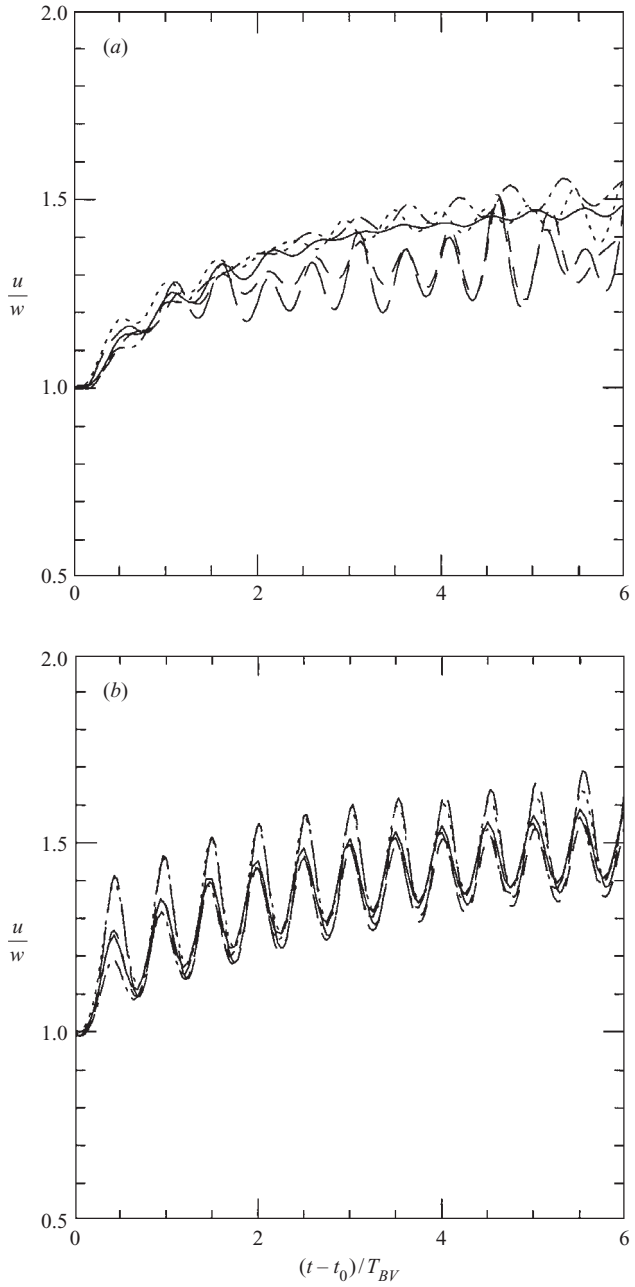

FIGURE 1. Ratio u/w of the horizontal and the vertical r.m.s. values of the velocity components. (*a*) DNS and (*b*) EDQNM$_2$ results for: ——, run R2; · · ·, run R1; – – – –, run A; — — — —, run B; — – — –, run r2.

1.45 for the lowest-viscosity calculations and of 1.5 for the other runs. This means that at the end of the computations, the flow contains more than twice the kinetic energy in each of the horizontal directions than in the vertical one.

The change in the growth of u/w at about $1.5T_{BV}$ is reproduced by the EDQNM2 model, but is not as clearly as in DNS. Assuming the independence of the ratio

u/w from the five values of the Brunt–Väisälä frequency and of the viscosity is not an artefact of the model, but a physical behaviour due to the statistical nature of the model; this is an interesting result for deriving universal one-point modelling at the level of the Reynolds stress tensor in stably stratified turbulence. This result deserves further investigation through the use of a broader range of values of N and ν. Finally, the main difference with DNS results lies in the prediction of larger oscillations of u/w (as also observed in § 5.2 for some length scales). The latter result, which appeared in Part 1 to be the major defect of the EDQNM$_2$ model for the present flow configuration, is due to an insufficient decorrelation between the vertical velocity and the temperature fluctuation.

Results from experiments on thermally stably stratified grid turbulence are in good agreement with the asymptotic value $u/w \simeq 1.5$. At the far end of their turbulent channel, Lienhard & Van Atta (1990) obtain a ratio that ranges between 1.56 and 1.72, and Yoon & Warhaft (1990) find slightly smaller values between 1.3 and 1.45, and with peaks up to 1.65. It is important to note that, in experiments, u/w settles to its maximal value in less than one Brunt–Väisälä period, whereas it takes more than two Brunt–Väisälä periods in our numerical results before reaching the value of 1.5. The reason lies in the specific initial conditions we have chosen, as recalled in § 4.1. Indeed, while the horizontal velocity component behaves identically in the present DNS and EDQNM$_2$ calculations and in the experiments of Lienhard & Van Atta (1990), the vertical velocity component behaves differently. In the laboratory experiments, the absence of potential energy just behind the grid yields a maximum decrease of the vertical velocity to a value which is 60% lower than the value w would have if the flow were unstratified. For the present initial condition where the reservoir of potential energy is greater than that of vertical kinetic energy, we have shown that a maximum decrease of the vertical kinetic energy of 30% of its isotropic value is still observed. It follows that the vertical kinetic energy decays less during the first Brunt–Väisälä period than in the laboratory experiments. It is remarkable that the same final value is still reached at the end of our computations. In the numerical simulations with initially zero potential energy (runs r3 and r4, not plotted), u/w reaches slightly higher values than for the non-zero case, as in the experiments (1.75 and 1.78 for $N = \pi$ and $\pi/2$ respectively).

We may combine this result with the fact that the ratio of vertical kinetic energy to potential energy is equal to 4/9, according to Part 1. This yields that 42% of the total energy of the flow is in the vortex part, against 33% at the initial time, while the remainder consists of wave motion. We also deduce that 72% of the horizontal kinetic energy is contributed by the vortex part, a result already found in Part 1. A useful implication for the next section is that the total kinetic energy is mainly contributed by its horizontal component, in a proportion of 82%. This energetic partition of the flow into wave and vortex parts very likely corresponds to some equilibrium state (possibly depending upon the initial conditions). Since the buoyancy force starts to influence all scales of motion from $1.5T_{BV}$, a model of linear interaction for the wave and vortex modes may be able to describe the flow dynamics from this time on. Following Hanazaki & Hunt (1996) and vanHaren, Staquet & Cambon (1996), it would therefore be useful to apply rapid distortion theory (RDT) to the flow, using as initial conditions the spectra of the velocity and temperature fields at $1.5T_{BV}$. RDT is, however, irrelevant for describing the initial stage ($t - t_0 < 1.5T_{BV}$) since, starting with our initial conditions at $t = t_0$, it would predict that u/w remains equal to 1 at all times.

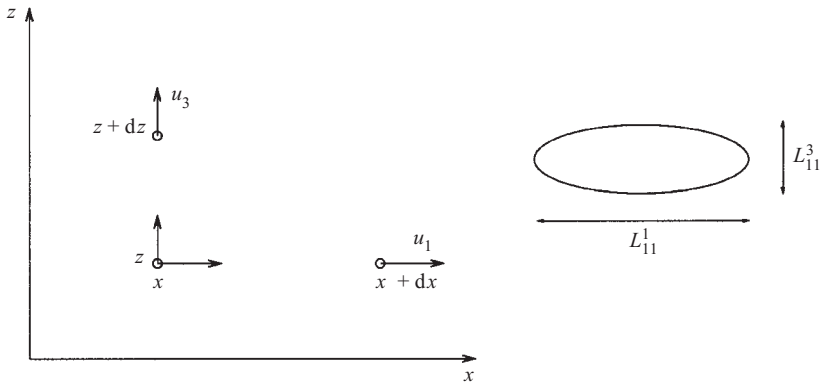

FIGURE 2. Integral length scales L_{ii}^{k} in the vertical ($k = 3$) and horizontal ($k = 1$) directions are defined using two-point correlations, respectively with vertical dz or horizontal dx separation. Correlations of either the vertical velocity component u_3 or the horizontal one u_1 are used. The resulting length scales may be used to characterize the size of turbulent structures of the flow, as schematically shown.

5.2. *Integral length scales*

5.2.1. *Definitions*

Large-scale structures in a stably stratified flow have lengths of different magnitude in the horizontal and vertical direction, because of the restoring effect of the buoyancy force. This has been known for a long time (e.g. Lin & Pao 1979) and our purpose here is to quantify the organization of the flow into layers by computing integral length scales related to correlations of velocity components with horizontal and vertical separation. These length scales are obtained in physical space by integrating the two-point longitudinal and transverse correlation functions (Batchelor 1953) (first equality below) or from spectra in Fourier space (second equality):

$$L_{ij}^{l} = \frac{1}{\overline{u_i u_j}} \int_0^\infty \langle u_i(\boldsymbol{x}) u_j(\boldsymbol{x} + \mathrm{d}\boldsymbol{x}_l) \rangle \, \mathrm{d}\boldsymbol{x}_l = \frac{\pi}{\overline{u_i u_j}} \int\int_{k_l=0} \langle \widehat{u_i u_j} \rangle (\boldsymbol{k}, t) \, \mathrm{d}^2 \boldsymbol{k}, \qquad (5.2)$$

where d$\boldsymbol{x}_l$ represents the separation distance in the lth direction. In homogeneous turbulence, an ergodic assumption permits computation of the ensemble average $\langle \ \rangle$ by a spatial average over the computational domain. A physical interpretation of these scales is provided in figure 2.

Projected onto the Craya–Herring frame of reference, the spectral integral in (5.2) yields for instance

$$L_{11}^{1} = \frac{4\pi}{\overline{u_1^2}} \int\int \Phi_1(\boldsymbol{k}) \, \mathrm{d}^3 \boldsymbol{k}.$$

In the following, we shall use axisymmetry to investigate only the L_{ii}^{l} with $(i, l) \in \{1, 3\}^2$. Of major importance are those related to horizontal components of the velocity, these contributing most to the kinetic energy, as shown in the previous section.

In freely decaying isotropic turbulence, these length scales behave identically in all three directions and longitudinal correlations ($i = l$ in the above definition), are exactly twice the transverse ones ($i \neq l$) (Batchelor 1953). They increase in time with a dependence that can be derived from dimensional arguments (see for instance Lesieur 1990, p. 195), of the form t^r. The exponent r depends upon the

behaviour of the kinetic energy spectrum at the lowest wavenumber ($k \to 0$); in our case, $E(k) \simeq k^4$ as $k \to 0$, and isotropic EDQNM theory yields $r = 0.31$. For two-dimensional turbulence, by contrast, Batchelor's theory predicts a linear evolution in time ($r = 1$) but laboratory and numerical experiments yield a value much closer to the three-dimensional exponent, namely $r \simeq 0.4$ (see e.g. Sommeria 2002).

5.2.2. Results

Figure 3 displays the time evolution of the horizontal and vertical correlation length scales of horizontal velocity, L_{11}^1 and L_{11}^3 respectively. Results for the statistical model and for DNS are shown for the five stratified runs. In figure 4, these length scales are normalized by the time-dependent corresponding isotropic lengths. Because u is mainly contributed by the vortex motion (more than 80%), L_{11}^1 characterizes the horizontal scale of this motion.

The time evolution of the integral length scales results from the decay of turbulence. Figure 3 thus shows that the correlation length L_{11}^1 increases with time, because energy is being dissipated at small scales. This signals that the horizontal scale of the vortex motion increases with time. Two regimes can be distinguished, a transition occurring again at about $1.5T_{BV}$. Before that time, the growth occurs at a higher rate than the isotropic rate: figure 4 indeed shows that the normalized length scale increases from a value of 1 from the initial time. Such behaviour was also found in the laboratory experiments of Yoon & Warhaft (1990, see their figure 7*a*), which were run for 0.6 Brunt–Väisälä periods at most. This result is surprising because, in our simulations, u decays like its isotropic counterpart up to $0.7T_{BV}$. This implies that the horizontal kinetic energy spectrum decays as in the isotropic case but is shifted faster toward the larger scales; consequently, the energy level of the small scales should be higher in the stratified case than in the isotropic one. One way to account for this assertion is to recall that a counter-gradient heat flux (that transfers potential energy into kinetic energy) exists at small scales, due to the stronger transfer rate of potential energy to small scales (Part 1). Figure 3 also shows that L_{11}^1 grows faster as N decreases. This behaviour was also observed in the laboratory experiments of Yoon & Warhaft (1990) (except for the largest value of N where the isotropic growth rate was recovered). The growth of the correlation length scales slows down from $1.5T_{BV}$ (see figure 3), which indicates a change in the largest-scale dynamics. Figure 4 shows that the longitudinal correlation scale evolves approximately as in three-dimensional isotropic turbulence because the ratio of scales is nearly constant (run R1) or slightly decays (run R2). However, because the growth rate in two-dimensional turbulence is very close to that in three dimensions, no clear conclusion about the large-scale flow dynamics can be inferred from this scale behaviour.

By contrast, the correlation along the vertical direction L_{11}^3 remains nearly constant from the initial time (except for the highest-viscosity run r2, in which L_{11}^3 grows by a factor 1.5 over the run, and for run B, where L_{11}^3 first rises to twice its initial value before slowly decaying). The initial value of L_{11}^3 coincides with the value of the Taylor microscale (but the latter scale grows by a factor 3 over the run duration). Figure 3 shows that, from $t - t_0 \simeq 1.5T_{BV}$, the temporal evolution follows that of isotropic turbulence, with half the level, but the dynamics at this scale is not that of three-dimensional turbulence, as explained below.

As sketched in figure 2, L_{11}^3 provides an estimate of the thickness of the vorticity layers that develop in the flow. Three basic processes control this thickness: viscous effects, since L_{11}^3 ranges between $\simeq$15 and a few Kolmogorov length scales between the beginning and the end of the computations; buoyancy effects, which dominate

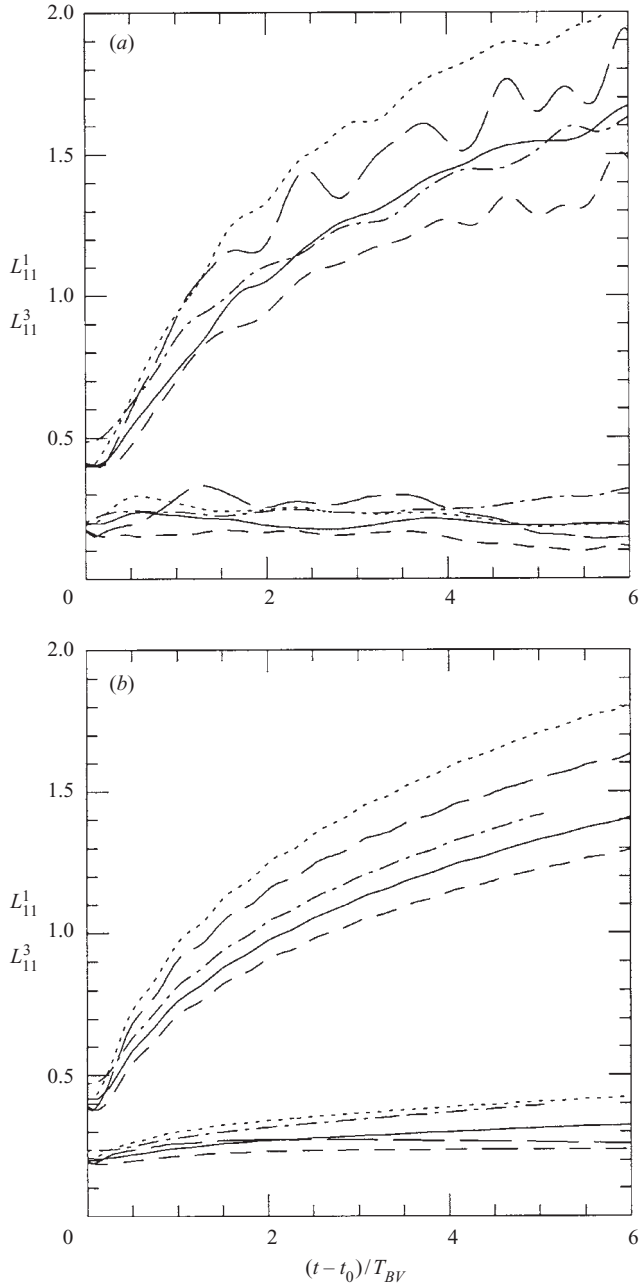

FIGURE 3. Integral length scales for the horizontal velocity component. (*a*) DNS and (*b*) EDQNM$_2$ results for: ———, run R2; ···, run R1; – – – –, run A; — — — —, run B; – – – – –, run r2. The top curves represent the growth of L_{11}^1 (correlation length in the horizontal plane), and the bottom curves show the evolution of L_{11}^3 (vertical correlation).

at all scales of motion from $(t-t_0)/T_{BV} \simeq 1.5$; and a straining motion due to the horizontal shear induced by the quasi-horizontal vortex motions. The time scales of these three effects are respectively $(L_{11}^3)^2/\nu$, N^{-1} and L_{11}^3/U; we shall again use $U = u$ as the scale of the horizontal velocity. We found that the two latter time scales are of

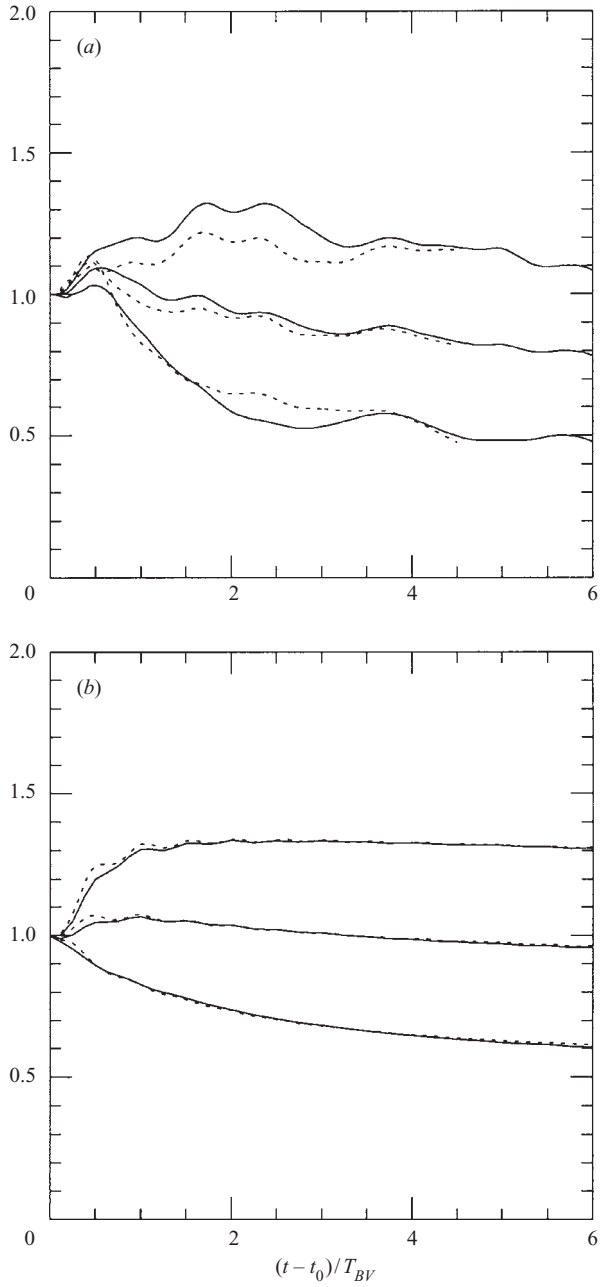

FIGURE 4. Ratio of the integral length scales $L^i_{11}(N)$ for the horizontal velocity component, in the stratified case, divided by the same quantity $L^i_{11}(N=0)$ obtained from the corresponding isotropic calculation. On each of the three of curves are shown the time evolution of: top curves: $L^{1*}_{11} = L^1_{11}(N)/L^1_{11}(N=0)$; bottom curves: $L^{3*}_{11} = L^3_{11}(N)/L^3_{11}(N=0)$; middle curves: the average value $(L^{1*}_{11} + L^{3*}_{11})/2$. The different sets correspond to: ———, run R2; · · ·, run R1. (*a*) DNS computations; (*b*) EDQNM$_2$ results.

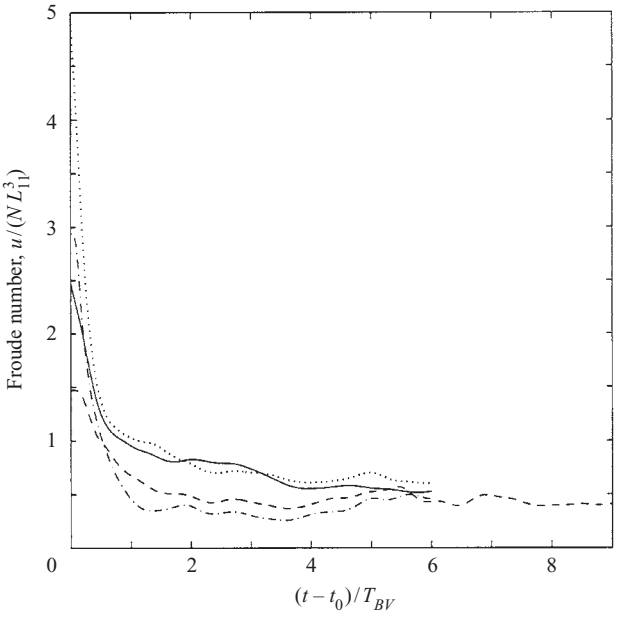

FIGURE 5. Froude number associated with the vorticity layers. DNS results : ——, run R2; · · ·, run R1; – – – –, run A; – · – · –, run B.

the same order and ten times smaller, in the mean, than the viscous time scale. This implies that the thickness of the layers is set by $L_{11}^3/u \simeq N^{-1}$. This relation amounts to writing that the Froude number $Fr = u/NL_{11}^3$ associated with L_{11}^3 is of order 1, consistently with our previous analysis (see § 4.1). In order to check this conjecture, we plot Fr as a function of $(t - t_0)/T_{BV}$ in figure 5 for the four runs R1, R2, A and B: all curves decay to a nearly constant value close to 0.5. The same behaviour is found for run r2 (not plotted for clarity) except that, from $2T_{BV}$, Fr starts decaying at a constant rate from the 0.6 value. Hence, $L_{11}^3 = 2u/N$ provides an estimate of the layer thickness for small enough viscosity. We note that this estimate matches the prediction of a dimensional analysis for inviscid fluid conducted by Billant & Chomaz (2001). We point out that these arguments are valid from $1.5T_{BV}$ only and, therefore, cannot account for the constant value of L_{11}^3 from the beginning of the run.

The simulations with zero initial potential energy (not shown) display the same behaviour as run r2, in which the viscosity ν has the same value. For instance, L_{11}^3 grows by 50% or so from its initial value to reach 0.32.

As shown on figure 3(b) for EDQNM$_2$ results, the statistical model predicts the L_{11}^3 growth inhibition as well. Also, the relative position of the curves for L_{11}^1 among the different runs is nearly the same as in DNS. Only the final value of L_{11}^1 at $t/T_{BV} = 6$ is found to be 15% smaller than in DNS. We note that the EDQNM$_2$ model does not reproduce the oscillatory behaviour displayed by the curves computed from DNS. Because correlation lengths in the statistical model are computed from the vortex-mode kinetic energy Φ_1, this means that no interaction exists at the largest scales between this mode and the wave mode in the model.

The evolution of the vertical longitudinal correlation length L_{33}^3 is plotted in figure 6. Since the contribution of the wave field to the w velocity component increases as time elapses, the longitudinal correlation is expected to oscillate, more so in the vertical direction. One can still discuss the evolution of this quantity on average, i.e. for the

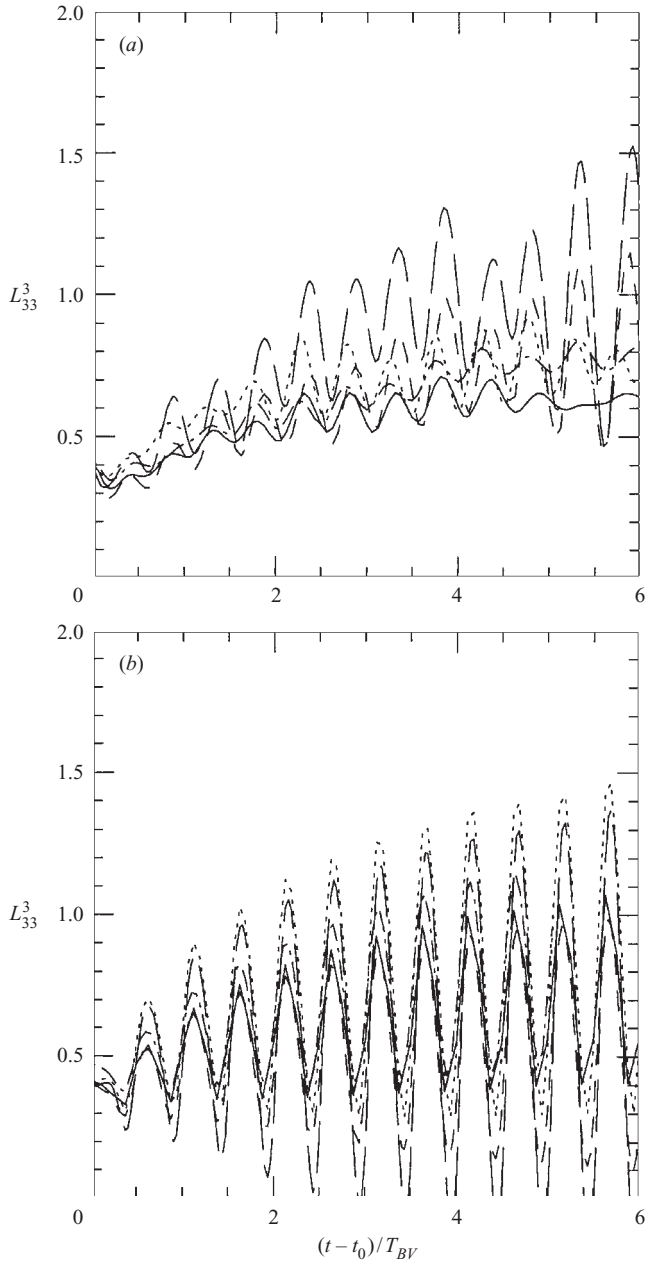

FIGURE 6. Integral length scale for the vertical velocity component, with vertical separation, L_{33}^3. (*a*) DNS and (*b*) EDQNM$_2$ results for: ——, run R2; · · ·, run R1; – – – –, run A; — — — —, run B; — · — · —, run r2.

mean value about which it oscillates. This mean value grows in time, unlike L_{11}^3, meaning that a stronger vertical correlation is present in the vertical fluid motion than in the horizontal motion. The growth rate of L_{33}^3 is however three times smaller than that of the longitudinal streamwise correlation L_{11}^1. It seems to reach a constant value, equal to about 0.7, as time elapses.

The same mean value is predicted by the EDQNM$_2$ model (figure 6*b*). However, the amplitude of the oscillations is overestimated by the model, the discrepancy being larger when N is lower, for reasons discussed in the previous section. The vertical correlation of w oscillates at nearly twice the Brunt–Väisälä frequency, meaning that w, which is mainly contributed by the wave field, oscillates at a frequency close N (since L^3_{33} is defined by a quadratic quantity). Hence, the waves propagate their energy vertically in the turbulent flow. A comparable result was observed by Hanazaki & Hunt (1996) using linear RDT theory.

These observations give the picture of the flow as superimposed quasi-horizontal layers with a strong vertical variability and subjected to wave deformation.

The normalized length scales $L^{l*}_{ii} = L^l_{ii}(N)/L^l_{ii}(N=0)$ are shown on figure 4. We should add to the previous comments on this figure that almost no dependence of the L^{l*}_{ii} is found on N in the EDQNM$_2$ model, unlike DNS. We also note that half the sum of L^{1*}_{11} and L^{3*}_{11} (middle curves on figure 4) remains very close to unity: this may be put in terms of a statistical volume conservation principle, such that the structures in the flow are incompressibly squeezed by stratification.

6. Small-scale anisotropy

6.1. *Definitions*

Of importance in stably stratified turbulence is the estimate of the dissipation rate of kinetic energy. This quantity is defined as $\epsilon = 2\nu\overline{s_{ij}s_{ij}}$ where $s_{ij} = (\partial u_i/\partial x_j + \partial u_j/\partial x_i)/2$ is the fluctuating rate of strain (Batchelor 1953); ϵ can be computed from experimental data but, for technical reasons, it usually contains only part of the velocity gradients present in the flow. In isotropic turbulence, only one velocity derivative is needed for obtaining the exact ϵ, e.g. $\epsilon = 15\nu\overline{(\partial u/\partial x)^2}$; ϵ can also be expressed using the isotropic relation $\overline{(\partial u/\partial x)^2} = \overline{(\partial v/\partial x)^2}/2$ between longitudinal and transverse gradients (Townsend 1976). However, in stably stratified turbulence, anisotropy that may arise at small scales implies that several gradients, if not all, should be used in order to estimate the dissipation. In axisymmetric flows only two directions need to be considered, namely horizontal and vertical.

Velocity gradients are easily computed in spectral space in DNS, of which we will only retain $\partial u/\partial x$, $\partial w/\partial x$, $\partial u/\partial z$, $\partial w/\partial z$; $\partial u/\partial y$ will also be retained for comparison with $\partial u/\partial x$. We shall compare their r.m.s. values $(\overline{(\partial u_i/\partial x_j)^2})^{1/2}$ with those obtained by the statistical model. In EDQNM$_2$ r.m.s. gradients are computed from energy density spectra, as follows.

From equation (2.4), the spectral components of the two-point velocity correlation tensor are obtained by projection of the Φ_i, $i = 1, 2$, onto the fixed frame of reference:

$$\hat{V}_{ij} = \Phi_1\left(e^1_i e^1_j\right) + \Phi_2\left(e^2_i e^2_j\right), \qquad (i, j) \in \{1, 2\}^2. \tag{6.1}$$

Moreover, the spectra of the velocity gradients are related to $\hat{\boldsymbol{V}}$, since $\widehat{\partial u_i/\partial x_j} = k_j\hat{u}_i$, by $\widehat{(\partial u_i/\partial x_j)(\partial u_i/\partial x_j)} = (k_j)^2\hat{V}_{ii}$ (no summation on i and j). Therefore, using definition (A 2), we obtain

$$\overline{\left(\frac{\partial u}{\partial x}\right)^2} = \frac{1}{2}\left[\int_0^\infty \int_0^{\pi/2} k^2 \sin^2\theta_k(\Phi_1 + \cos^2\theta_k\ \Phi_2)\,\mathrm{d}\theta_k\,\mathrm{d}k\right], \tag{6.2}$$

$$\overline{\left(\frac{\partial u}{\partial z}\right)^2} = \frac{1}{2}\left[\int_0^\infty \int_0^{\pi/2} k^2 \cos^2\theta_k (\Phi_1 + \cos^2\theta_k\ \Phi_2)\,\mathrm{d}\theta_k\,\mathrm{d}k\right], \tag{6.3}$$

$$\overline{\left(\frac{\partial w}{\partial x}\right)^2} = \frac{1}{2}\left[\int_0^\infty \int_0^{\pi/2} k^2 \sin^4\theta_k\ \Phi_2\,\mathrm{d}\theta_k\,\mathrm{d}k\right], \tag{6.4}$$

$$\overline{\left(\frac{\partial w}{\partial z}\right)^2} = \left[\int_0^\infty \int_0^{\pi/2} k^2 \cos^2\theta_k \sin^2\theta_k\ \Phi_2\,\mathrm{d}\theta_k\,\mathrm{d}k\right]. \tag{6.5}$$

Note that $\Phi_1 + \cos^2\theta_k\ \Phi_2$ is twice the horizontal kinetic energy spectrum, and $\sin^2\theta_k\ \Phi_2$ twice the vertical kinetic energy spectrum. As expected, the horizontal vortex mode spectrum Φ_1 only contributes to horizontal motion, but the waves contribute to the vertical motion as well. The sum of the above four terms multiplied by 2ν equals ϵ.

6.2. *Results*

Using the previous definitions, the different velocity gradients obtained from DNS and EDQNM$_2$ are plotted on figures 7 and 8, for runs R1 and R2. The behaviour of the resulting dissipation rate of kinetic energy ϵ was commented on in Part 1.

Since r.m.s. values are plotted in figures 7 and 8 and the initial flow is isotropic, $\partial u/\partial x$ and $\partial w/\partial z$ differ by a factor $\sqrt{2}$ from $\partial u/\partial y$, $\partial u/\partial z$ and $\partial w/\partial x$. The figures show that the strongest departure from isotropy occurs in $\partial u/\partial z$, from $0.1T_{BV}$ for $N = \pi$ and from $0.3T_{BV}$ for $N = \pi/2$. The longitudinal gradient $\partial w/\partial z$ departs from isotropy from this time on as well. Another striking feature is that $\partial u/\partial y$ remains nearly equal to $\partial w/\partial x$ at all times, their level being matched by $\partial w/\partial z$ up to $2T_{BV}$. We also note that the weakest gradient $\partial u/\partial x$ decays from this time on at the same rate as these three gradients, the difference amounting to a factor of 1.2. Finally, the dominance of the transverse gradient $\partial u/\partial z$ over the other gradients increases as time elapses. It follows that, from $t \simeq 1.5T_{BV}$, one may write

$$1.2\ \partial u/\partial x\ \simeq\ \partial u/\partial y\ \simeq\ \partial w/\partial x\ \simeq\ \partial w/\partial z\ <\ \partial u/\partial z. \tag{6.6}$$

Part of these relations can be easily accounted for. As time elapses, the horizontal kinetic energy becomes dominated by the vortex motion, which involves quasi-horizontal large-scale structures. Thus $\partial u/\partial x$ should remain weak after these structures have emerged from the initial turbulent state, that is, from $t - t_0 \simeq 1.5T_{BV}$. Also, the reduction of the length scale in the vertical direction by stratification implies that vertical gradients should dominate. In order to account for the dominance of $\partial u/\partial z$ over $\partial w/\partial z$, let us estimate their order of magnitude: $\partial u/\partial z \sim u/L_{11}^3$ while $\partial w/\partial z \sim w/L_{33}^3$; thus $(\partial u/\partial z)/(\partial w/\partial z) \sim (u/w)/(L_{11}^3/L_{33}^3)$. But $u/w > 1$ (from figure 1) while $L_{11}^3/L_{33}^3 < 1$ (from figures 3*a* and 6*a*), so that the vertical gradient of u dominates that of w (by a factor 2 or so according to figure 7). The overall dominance of $\partial u/\partial z$ confirms the organization of the flow into quasi-horizontal layers whose relative motion results in this horizontal shear. A visualization of a constant surface $\partial u/\partial z$ at 6 Brunt–Väisälä periods, displayed in figure 9, demonstrates this organization. That $\partial u/\partial z$ should dominate the velocity gradients in a stably stratified fluid, and therefore control the dissipation rate of kinetic energy, was first realized by Lilly (1983), using the wave–vortex decomposition of Riley *et al.* (1981). This conjecture has been given a quantitative basis by Fincham *et al.* (1996), who found that the shear associated with the flow layering accounts for 90% of the kinetic energy dissipation. This result will be further discussed in the next section.

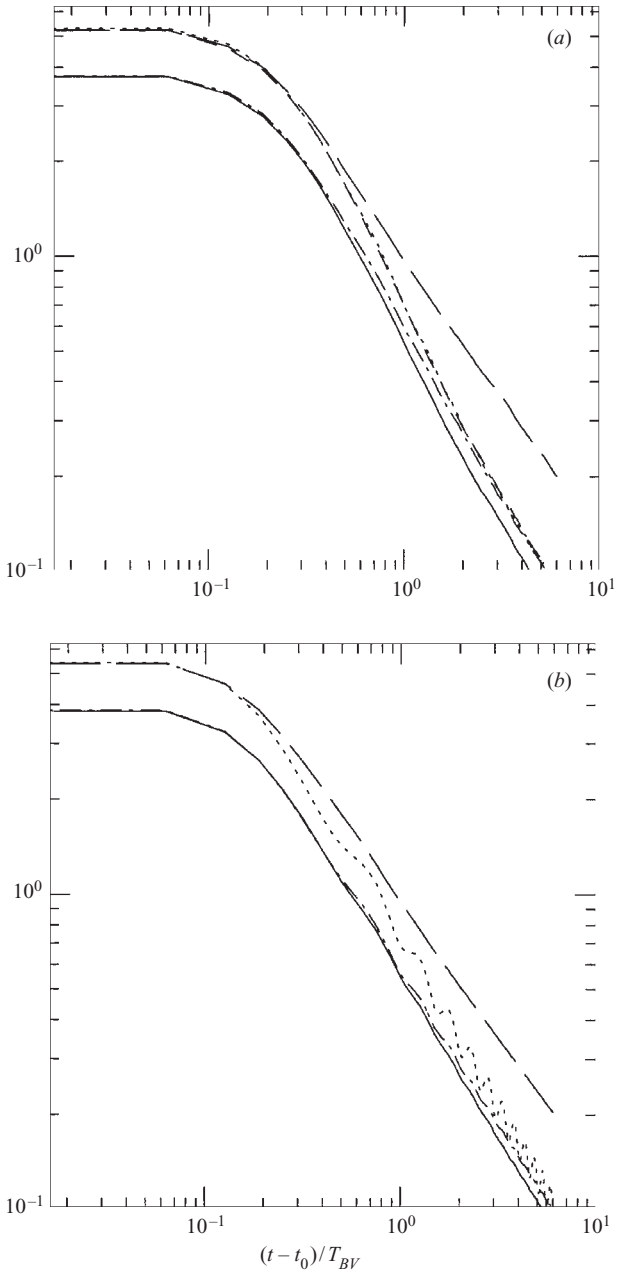

FIGURE 7. Root-mean-square values of the velocity gradients $\partial u_i/\partial x_j$, for run R1, given (*a*) by DNS, (*b*) by the EDQNM$_2$ model. ——, $\partial u/\partial x$; $\cdots$, $\partial w/\partial x$; – – – –, $\partial u/\partial y$; – – – –, $\partial u/\partial z$; – – · – –, $\partial w/\partial z$. ($\partial u/\partial y$ is not plotted for the EDQNM$_2$ model because it is equal to $\simeq\partial w/\partial x$ due to axisymmetry).

We have already noticed that the frequency of the waves is close to N: assuming this global property also holds locally, this means that the fluid particles oscillate in a direction close to the vertical, thus inducing a horizontal shear $\partial w/\partial x$ (or $\partial w/\partial y$). According to relations (6.6), this shear is rather strong because it is of the same order

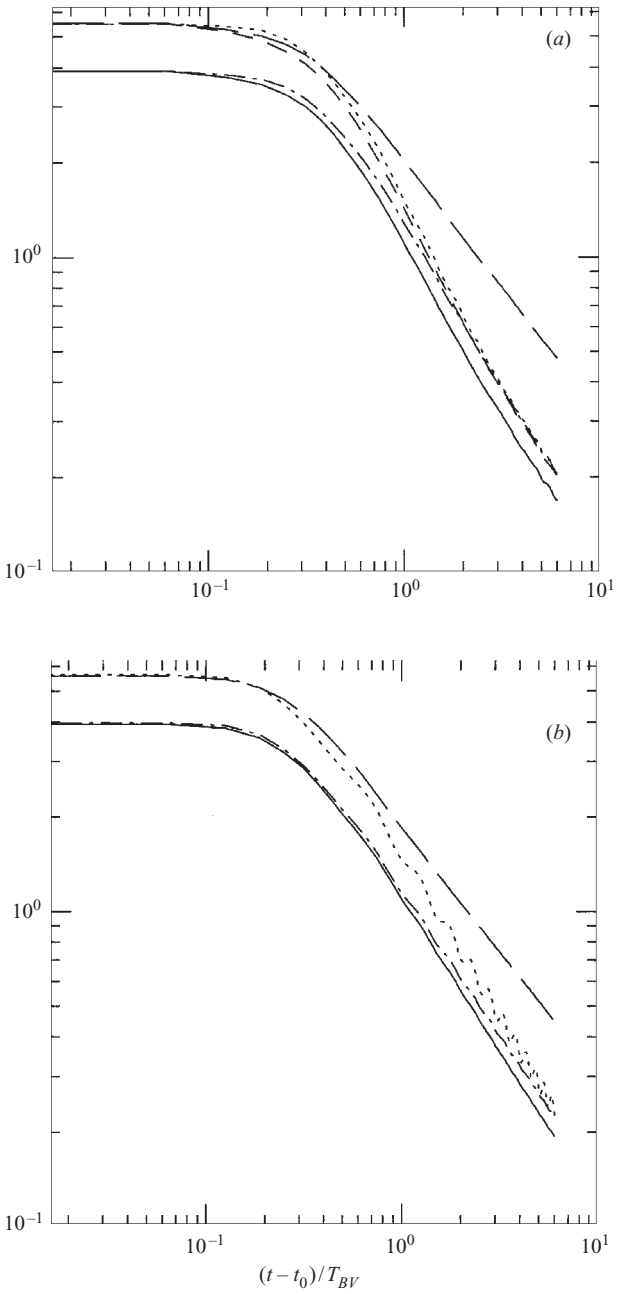

FIGURE 8. Root-mean-square values of the velocity gradients $\partial u_i/\partial x_j$, for run R2, given (*a*) by DNS, (*b*) by the EDQNM$_2$ model. See figure 7 for the meaning of the line types.

as the vertical vorticity of the flow, $\simeq \partial u/\partial y$, but still smaller than that resulting from the vertical variability of the vortex motion, $\partial u/\partial z$. Finally, relations (6.6) indicate that the flow is nearly isotropic in the horizontal plane although only one realization is considered: again, isotropy would imply $\partial u/\partial x$ to be smaller by a factor $\sqrt{2}$ than $\partial u/\partial y$ whereas this factor is equal to 1.2 instead.

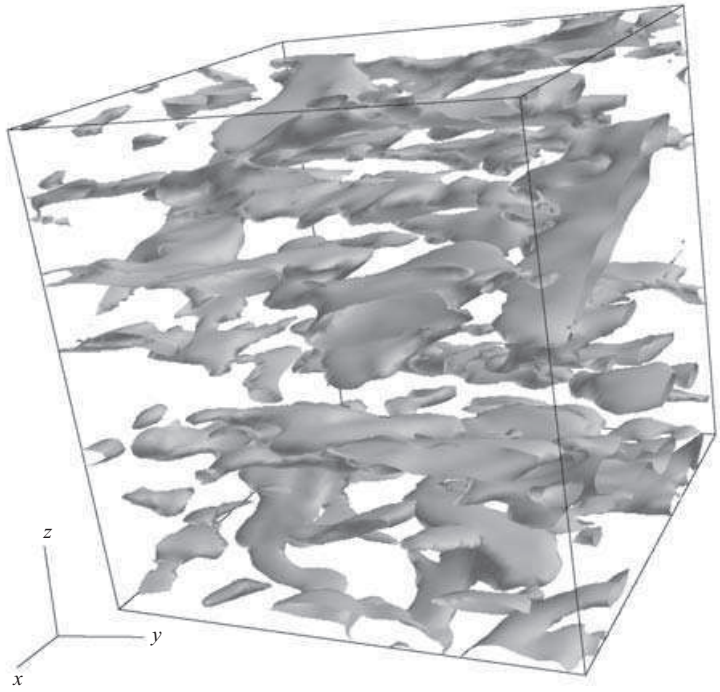

FIGURE 9. Surface of $\partial u_2/\partial z$ equal to 25% of its maximum value in the computational box, for run R1 at $(t - t_0)/T_{BV} = 6$.

We observe on figures 7(*b*) and 8(*b*) that the EDQNM$_2$ predicted values for the gradients are in good agreement with the DNS results. The evolution of the largest gradient, $\partial u/\partial z$, is very close to that of DNS, with almost the same value at $6T_{BV}$. The smallest gradient $\partial u/\partial x$ is slightly overestimated by the statistical model at this time. The closing together of $\partial w/\partial x$ and $\partial w/\partial z$ is also observed in figures 7(*b*) and 8(*b*), but occurs a little later than in the numerical simulations. The vertical gradient displays unwanted oscillations whose origin is the same as that resulting in the overly large oscillations observed in § 5.2 for L_{33}^3. The EDQNM$_2$ model, despite its statistical nature, can therefore reproduce much of the mechanisms that lead to the localized organization of the flow. This overall good agreement with DNS should be underlined, especially with respect to $\partial u/\partial z$, indicating a good prediction of the layering of the flow by the model.

As in Thoroddsen & Van Atta (1992), we plot in figure 10 the evolution of the ratio $\mathscr{R} = \overline{(\partial w/\partial x)^2}/\overline{(\partial u/\partial x)^2}$ as a function of $(t - t_0)/T_{BV}$. This ratio is a measure of the anisotropy between horizontal gradients of vertical and horizontal velocity. Starting from 2, as expected in isotropic turbulence, it decreases to an average value of $\simeq$1.5 – that is, 1.2^2 according to relations (6.6) – at $6T_{BV}$. The curves for runs R1 and R2, computed by DNS or predicted by the statistical model collapse on a single curve after the first Brunt–Väisälä period or so, apart from stronger oscillations in the EDQNM$_2$ model. This is consistent with the results of Thoroddsen & Van Atta (1992), which collapse on a single curve when plotted as a function of t/T_{BV} from $0.5T_{BV}$. In these laboratory experiments, $\mathscr{R}$ also seems to tend toward an asymptotic value for the highest value of N, but this value is half ours, being equal to $\simeq$0.7. This discrepancy may be due to the difference in initial condition: results for the zero

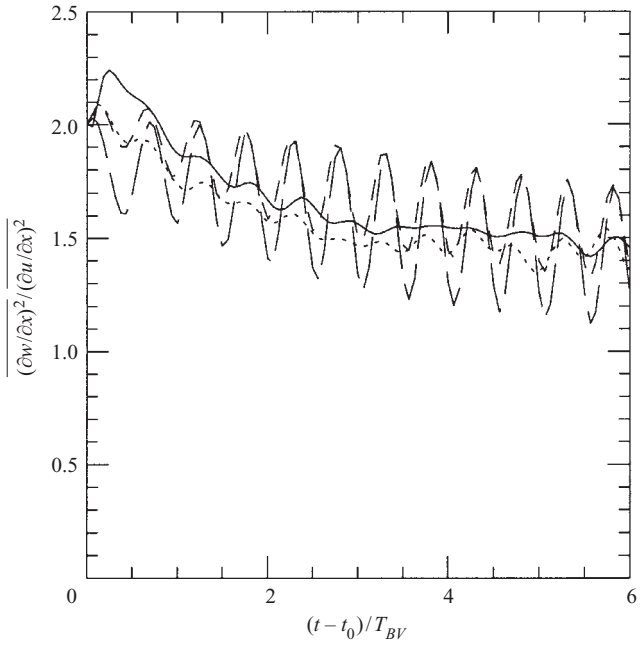

FIGURE 10. Ratio $\overline{(\partial w/\partial x)^2}/\overline{(\partial u/\partial x)^2}$. Run R2: ——, DNS; – – – –, EDQNM$_2$ model. Run R1: – – – –, DNS; — — — —, EDQNM$_2$ model.

initial potential energy runs (not displayed) show that (i) the two curves collapse from the beginning of the run, and (ii) they decrease steadily and reach a value close to 1.2 at $3T_{BV}$. It should be noted that Thoroddsen & Van Atta (1992) also compared their experimental results with those of Riley *et al.* (1981) (which agree with ours), up to $1.25\,T_{BV}$.

Finally, the asymptotic value of $\mathscr{R}$ in our DNS allows us to infer an estimate of the scale of the waves in the x-direction. We characterize this scale by the transverse correlation length scale of w, L^1_{33}. As above, $\mathscr{R} \sim (w/u)/(L^1_{11}/L^1_{33})$ so that the asymptotic value $\mathscr{R} \simeq 1.5$ yields $L^1_{33} \simeq 1.8 L^1_{11}$. This simple argument, if accurate enough, would yield that the horizontal scale of the waves is smaller by at most only a factor 2 than that of the vortex motions.

6.3. *Dissipation models*

Modelling the dissipation rate of kinetic energy is of crucial importance in oceanography because most models for small-scale mixing rely upon ϵ. The appropriateness of the isotropic formula for calculating ϵ in the thermocline has been addressed by Yamazaki & Osborn (1990, 1993*a*, *b*) using *in situ* measurements. These authors report that, according to the measurements of Gargett *et al.* (1984), the isotropic formula can be used when $\epsilon/\nu N^2$ is larger than 200. In the thermocline however, $\epsilon/\nu N^2$ is lower than 200, meaning that stratification effects should be accounted for. This led Yamazaki & Osborn (1990, 1993*a*, *b*) to express ϵ using the theory of axisymmetric turbulence about the vertical direction. Following Batchelor (1946), this expression is

$$\epsilon_A = \nu \left(6 \overline{\left(\frac{\partial u}{\partial y}\right)^2} - 5 \overline{\left(\frac{\partial w}{\partial z}\right)^2} + 2 \overline{\left(\frac{\partial w}{\partial x}\right)^2} + 2 \overline{\left(\frac{\partial u}{\partial z}\right)^2} \right). \tag{6.7}$$

The data in the thermocline were obtained from a submarine so that only two cross-stream gradients were available, $\partial w/\partial x$ and $\partial v/\partial x$. Approximations for ϵ_A were thus made, yielding an upper and a lower bound for this rate:

$$\epsilon_A^l = \nu\left(\frac{11}{2}\overline{\left(\frac{\partial v}{\partial x}\right)^2} + 2\overline{\left(\frac{\partial w}{\partial x}\right)^2}\right), \qquad \epsilon_A^u = \nu\left(8\overline{\left(\frac{\partial v}{\partial x}\right)^2} - \frac{1}{2}\overline{\left(\frac{\partial w}{\partial x}\right)^2}\right). \tag{6.8}$$

Both approximations were found to compare reasonably well with the isotropic formulae, the maximum error being 40%. This led Yamazaki & Osborn (1990, 1993*a*, *b*) to conclude that isotropic formulae work well in the thermocline even if the flow is not isotropic, given the uncertainty in the current oceanographic technique.

A semi-isotropic expression for ϵ had been proposed by Stillinger, Helland & Van Atta (1983), based upon two velocity gradients measured in a salt-stratified water tunnel:

$$\epsilon_S = \nu\left(10\overline{\left(\frac{\partial u}{\partial x}\right)^2} + \frac{5}{2}\overline{\left(\frac{\partial w}{\partial x}\right)^2}\right). \tag{6.9}$$

Thoroddsen & Van Atta (1992) applied the three approximations (6.8)–(6.9) to their experimental data and found a large discrepancy between their predictions, namely $\epsilon_A^l \simeq \epsilon_A^u = \epsilon_S/2 = \epsilon_{iso}/2.5$ (ϵ_{iso} is the isotropic expression for ϵ based upon one gradient only). The reason is very probably the explicit absence of the horizontal shear $\overline{(\partial u/\partial z)^2}$ in these approximations. Indeed, in the laboratory experiments of Itsweire, Helland & Van Atta (1986), expression (6.9) allowed the turbulence energy equation to be closed within an error of 5% but a strong internal wave field was detected, unlike most wind tunnel experiments.

The first laboratory experiments where the vertical gradient of a horizontal velocity component was measured were those of Fincham *et al.* (1996), at high Reynolds number; ϵ was found to be very well predicted by considering only the horizontal shear since the approximation

$$\epsilon^\infty = 2\nu\overline{(\partial u/\partial z)^2} \tag{6.10}$$

accounted for 90% of the decay rate of the kinetic energy for t/T_{BV} larger than $\simeq$7. The internal wave field appeared to be very weak in these experiments.

In the following, we examine the validity of these different approximations for our numerical data, for $(t - t_0)/T_{BV}$ larger than 2. Relations (6.6) between the velocity gradients will thus be used. The ratio of the actual (numerically computed) dissipation rate to the isotropic one was found in Part 1 to increase linearly with time for $t/T_{BV} > 1.5$, from 0.7 to 1.5, so that an isotropic formula cannot be accurately used in the present case.

We first consider the approximations proposed by Yamazaki & Osborn (1990, 1993*a*, *b*) and Stillinger *et al.* (1983). Interestingly, the upper and lower bounds of the former approximations yield the same expression $\epsilon_A^u = \epsilon_A^l = 7.5\nu\overline{(\partial u/\partial y)^2}$, while the latter approximation yields $\epsilon_S \simeq 9.5\nu\overline{(\partial u/\partial y)^2}$. For our data, the expression for ϵ_S leads to a 50% underestimation of the dissipation at the end of the computations so that the Yamazaki & Osborn expression will not yield a satisfactory prediction

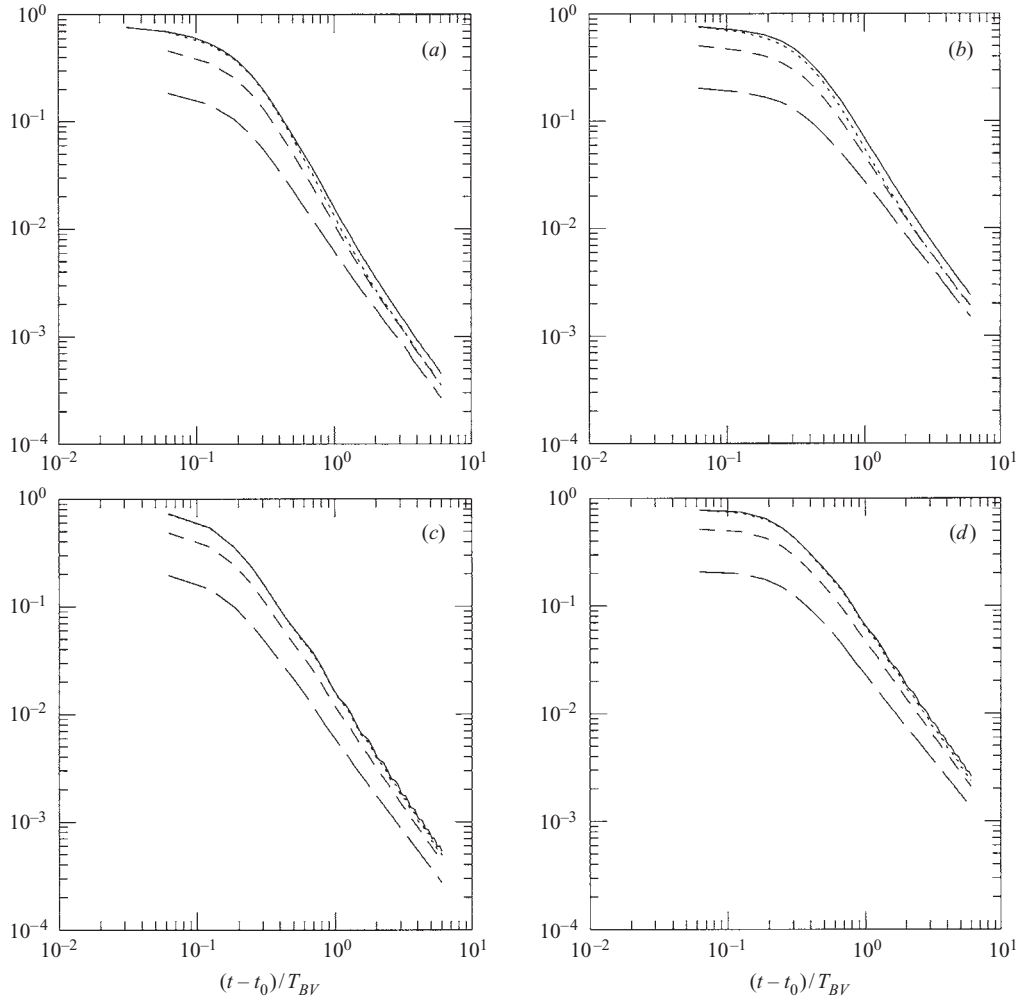

FIGURE 11. Dissipation rate of kinetic energy ϵ (———), along with the approximations ϵ_A ($\cdots$) (axisymmetric expression), $\tilde{\epsilon}_A$ (– – – –) (axisymmetric expression using relations (6.6) and ϵ_∞ (— — — —) (defined by (6.10)). DNS results for: (*a*) run R1, (*b*) run R2. EDQNM model: (*c*) run R1, (*d*) run R2.

either. Using relation (6.6) again, ϵ_A becomes

$$\tilde{\epsilon}_A = \nu \left(3 \overline{\left(\frac{\partial u}{\partial y} \right)^2} + 2 \overline{\left(\frac{\partial u}{\partial z} \right)^2} \right). \tag{6.11}$$

Since the ratio of the two gradients in (6.11) decreases as time elapses, it is useful also to consider the approximation ϵ^∞ used by Fincham *et al.* (1996). Figure 11 thus displays the actual dissipation rate ϵ along with the approximations ϵ_A, $\tilde{\epsilon}_A$ and ϵ^∞. For runs R1 and R2, $\tilde{\epsilon}_A$ provides a very good prediction of ϵ_A for $(t - t_0)/T_{BV} > 2$, as expected, and accounts for 87% of ϵ. (The prediction is obviously better for the EDQNM$_2$ model, because of exact axisymmetry in the model.) At the end of the DNS, ϵ_∞ accounts for only 60% of ϵ, possibly because the internal wave field is not

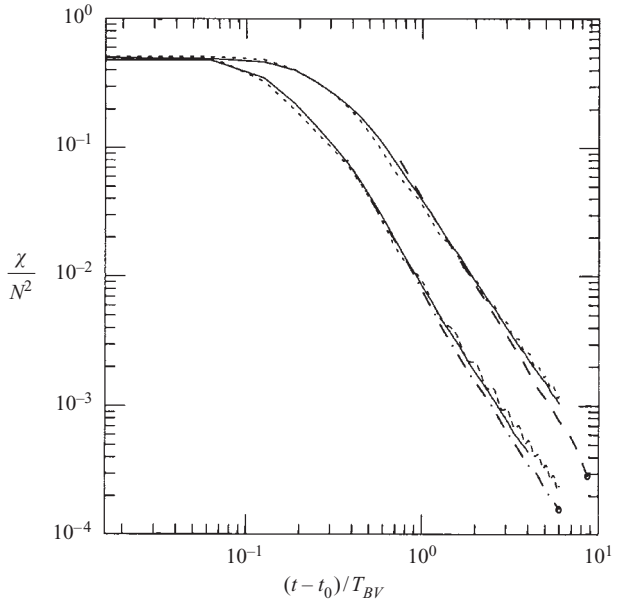

FIGURE 12. Dissipation rate of half the fluctuating temperature variance divided by N^2, χ/N^2. DNS versus EDQNM$_2$ model for runs R1 and R2. ———, DNS; – – – –, EDQNM$_2$ model. Top set of curves correspond to run R2, lower ones to run R1. DNS only for (– – – –), run A; — – — –, run B (both marked with ○ at end for better identification). All dissipation rates scale as $\sim t^{-2}$ after one Brunt–Väisälä period.

weak in our computations. For the EDQNM$_2$ model, ϵ_∞/ϵ is equal to 55% at $6T_{BV}$ of run R1 as well as at the end of run R2.

6.4. *Scalar dissipation*

Let χ be the dissipation rate of half the variance of the fluctuating temperature $\overline{T^2}/2$; χ is thus defined as

$$\chi = \kappa \left[\overline{\left(\frac{\partial T}{\partial x}\right)^2} + \overline{\left(\frac{\partial T}{\partial y}\right)^2} + \overline{\left(\frac{\partial T}{\partial z}\right)^2} \right]. \tag{6.12}$$

When the fluid is uniformly stratified, the quantity $\overline{T^2}/(2N^2)$ is a good approximation for the available potential energy (Holliday & McIntyre 1981). Thus, χ/N^2 is the dissipation rate of available potential energy.

The quantity χ/N^2 is plotted in figure 12 for DNS and for the EDQNM$_2$ model. In the model, horizontal and vertical temperature gradients have been computed from axisymmetric spectra in the EDQNM$_2$ model as:

$$\overline{\frac{\partial T}{\partial x}^2} = \overline{\frac{\partial T}{\partial y}^2} = \frac{1}{2}\int k^2 \sin^2\theta_k \Phi_3 \, \mathrm{d}^3\boldsymbol{k}, \qquad \overline{\frac{\partial T}{\partial z}^2} = \int k^2 \cos^2\theta_k \Phi_3 \, \mathrm{d}^3\boldsymbol{k}.$$

Figure 12 shows that the EDQNM$_2$ model follows quite closely the power law found in the numerical simulations, to better than 1%, with an exponent of decay close to 2. Only very small oscillations are present in the EDQNM$_2$ predictions.

For the purpose of the mixing study reported in the next section, we compare the quantity χ/N^2 for the four high-resolution DNS (R1, R2, A and B), also displayed in figure 12. Two striking features are apparent: (i) the transition at $1.5T_{BV}$, from which

small scales become affected by buoyancy force, is clearly visible in run B and, to a lesser extent, in run A as well (note that run B corresponds to the most turbulent flow that we simulated, because it has the lowest viscosity and Brunt–Väisälä frequency); (ii) χ/N^2 in runs A and B decays from this time on and eventually becomes lower than in runs R2 and R1 respectively. This behaviour should be attributed to the counter-gradient heat flux that exists at small scales, which leads to a re-stratification of the flow.

The time evolution of the r.m.s. values of the horizontal and vertical gradients of T is plotted in figure 13, as computed from DNS and the EDQNM$_2$ model, for run R2 (a) and for run R1 (b). The figure again shows that axisymmetry is satisfied well in DNS. The temperature gradients in the horizontal and vertical directions start to separate at the very early stage of the evolution, at about $(t - t_0)/T_{BV} \simeq 0.2$. Thus, anisotropy appears to develop in the temperature gradients nearly as fast as for the velocity components. The stronger transfer of potential energy toward small scales (which makes the vertical kinetic energy decrease and creates small-scale temperature fluctuations at the same time) occurs again. We still note that the decay rate is slower at the beginning of the computation for the strongest stratified run (figure 13a), than for run R1 for which $N = \pi/2$ (figure 13b). Nonlinear effects are active during this earlier stage as just mentioned, which accounts for the decay process, but the inhibiting effect of stratification already has an influence on these gradients, which accounts for the smaller decay of run R2. The gradients in the vertical direction next decay slower than horizontal ones, signalling that the temperature field, like the kinematic field, develops a layered structure with vertical variability. Note that the gradients recover the same decay rate in both runs, unlike their early evolution, indicating that the small-scale dynamics eventually becomes influenced by buoyancy effects.

Results for the EDQNM$_2$ model are also displayed on figure 13. With respect to the separation of the vertical and horizontal gradients, the model is in very good agreement with DNS results. The value of $\partial T/\partial z$ at $t/T_{BV} = 6$ is exactly the same, although a small difference is observed at the beginning of the decay in the strongly stratified case. The faster decrease of the derivative $\partial T/\partial x$ is predicted well by the statistical model, despite a small difference, at the end of the computation, with the DNS value. We note that $\partial T/\partial x$ oscillates noticeably, as a result of wave activity.

The anisotropy of the small temperature scales can be quantified by the ratio (e.g. Thoroddsen & Van Atta 1996)

$$\mathscr{R}' = \overline{(\partial T/\partial z)^2}/\overline{(\partial T/\partial x)^2}. \tag{6.13}$$

$\mathscr{R}'$ is plotted as a function of $(t - t_0)/T_{BV}$ in figure 14, for DNS runs only: R1 and R2, as well as the zero initial potential energy runs r3 and r4. $\mathscr{R}'$ starts from the isotropic value of 1 (for runs r3 and r4, both gradients vanish at $t = t_0$ so that $\mathscr{R}'$ is undefined). The striking feature is that all curves behave similarly, apart from stronger oscillations for r3 and r4. The figure shows that about 2.5 Brunt–Väisälä periods are needed for anisotropy of the temperature gradients to fully develop. A constant value of about 3 is eventually reached for runs R1 and R2 and it is very likely that this same value would be reached in runs r3 and r4.

The ratio $\mathscr{R}'$ was also inferred from experimental measurements by Thoroddsen & Van Atta (1996). $\mathscr{R}'$ was found to increase as well, from the value of about 1 close to the grid and to attain a value of order 2.2 (for the highest value of N) after 1.2 Brunt–Väisälä periods, a time limit imposed by the length of the tunnel. This is in agreement with our DNS results, whatever the initial condition. The structure of the

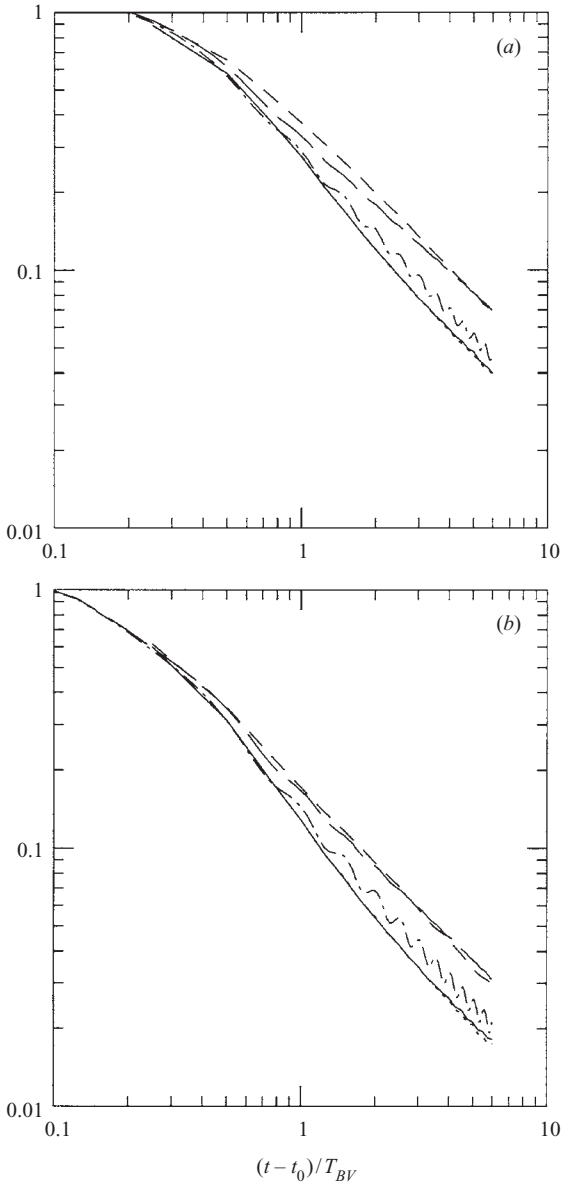

FIGURE 13. Root-mean-square values of the temperature derivatives in the horizontal and vertical directions, non-dimensionalized by their value at $t = t_0$, given by the simulation and the model: (*a*) run R2; (*b*) run R1. ——, horizontal x DNS derivative; ···, horizontal y DNS derivative; – – – –, horizontal EDQNM derivative; – – – –, vertical DNS derivative; — — — —, vertical EDQNM_2 derivative.

temperature field therefore might relax toward the same state independently of the initial conditions. It is noteworthy that we were able to draw the same conclusion for the ratio u/w. (The asymptotic value may however depend upon the Prandtl number.)

The existence of such an asymptotic value for the dissipation rate of the temperature variance implies that a simple expression, based upon knowledge of one gradient only, can be derived. Indeed, axisymmetry yields $\overline{(\partial T/\partial x)^2} = \overline{(\partial T/\partial y)^2}$ to a good

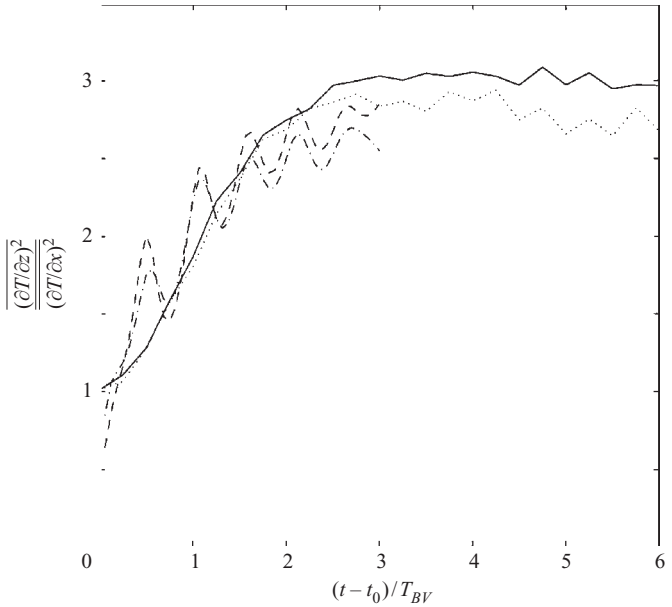

FIGURE 14. Ratio of the mean-square values of temperature derivatives in the horizontal and vertical directions, $\overline{(\partial T/\partial z)^2}/\overline{(\partial T/\partial x)^2}$, computed by DNS only. ———, run R2; · · ·, run R1; – – – –, run r3; – · – · –, run r4.

approximation and, from figure 14, $\overline{(\partial T/\partial x)^2} = \alpha\ \overline{(\partial T/\partial z)^2}$, with $\alpha \simeq 1/3$ for run R2 and $\alpha \simeq 1/2.8$ for run R1 and for the EDQNM$_2$ model. It follows that χ may be expressed as

$$\tilde{\chi} = (2\alpha + 1)\kappa\ \overline{(\partial T/\partial z)^2}, \tag{6.14}$$

for $t/T_{BV} > 2$.

7. Mixing

7.1. *Vertical turbulent diffusivity and Cox number*

The estimation of mixing in a stably stratified fluid has profound geophysical implications. For instance, the mixing processes are parameterized through a vertical eddy diffusivity in large-scale oceanic circulation models, and the long-term predictions of these models have been shown to be very sensitive to this parameterization (as mentioned in the Introduction).

In a stably stratified fluid, mixing is driven by the large energetic scales of the flow but eventually results from molecular diffusion. Mixing processes therefore involve the smallest dynamical scales, through temperature gradients. The restoring action of the buoyancy force implies that vertical transport in a stably stratified fluid can only occur through mixing. Fluid particles would return to their equilibrium position in a perfect fluid. Mixing is thus most often quantified through a vertical (actually diapycnal) turbulent diffusivity defined as

$$\text{vertical turbulent diffusivity } (z) \ = \ \frac{\text{turbulent diffusive flux of temperature}}{\text{mean temperature gradient}}, \tag{7.1}$$

where the numerator and denominator represent horizontally averaged quantities.

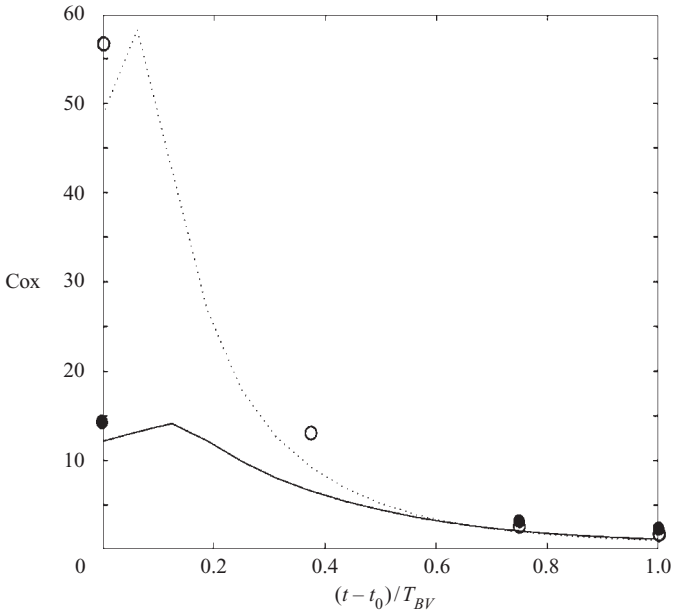

FIGURE 15. Cox number computed from DNS; ———, R2; ···, run R1; ●, run A; ○, run B. (The data are sparse for runs A and B, which are therefore indicated with symbols only.)

A common difficulty in mixing studies is to estimate the turbulent diffusive flux of temperature, or its vertical average, and several models have been proposed for this purpose (see e.g. Toole 1998 for a review). In the present case of uniformly stratified fluid in the Boussinesq approximation, its vertical average can be very well approximated by χ/N^2, while the mean temperature gradient remains very close at all times to the linear gradient N^2 (we recall that T is scaled like an acceleration). Hence, χ/N^2 also represents the rate of change of potential energy due to turbulent mixing processes. The vertically averaged turbulent vertical diffusivity is therefore defined as

$$K_d = \frac{\chi}{N^4}, \tag{7.2}$$

which is the well-known Osborn–Cox model (Osborn & Cox 1972). A generalization of this definition to non-homogeneous stably stratified fluids has been derived by Winters *et al.* (1995), using the concept of minimal potential energy developed by Lorenz (1955) and Thorpe (1977).

The vertical diffusivity K_d normalized by the molecular diffusivity κ defines the Cox number:

$$\mathrm{Cox} \equiv \frac{K_d}{\kappa} = \frac{\chi}{\kappa N^4}.$$

Normalization by κ gives the departure from molecular diffusion due to nonlinear and buoyancy effects.

The Cox number is plotted as a function of $(t - t_0)/T_{BV}$ in figure 15 up to one Brunt–Väisälä period, for runs R1, R2, A and B. The data collapse on a single curve from $(t - t_0)/T_{BV} \simeq 0.6$, signalling that vertical transport becomes controlled by the accumulated effect of buoyancy from this time on. Such a unique dependence on t/T_{BV} was also found by Yoon & Warhaft (1990) (from $t/T_{BV} \simeq 0.35$) and by Lienhard & Van Atta (1990) (from $t/T_{BV} \simeq 0.2$).

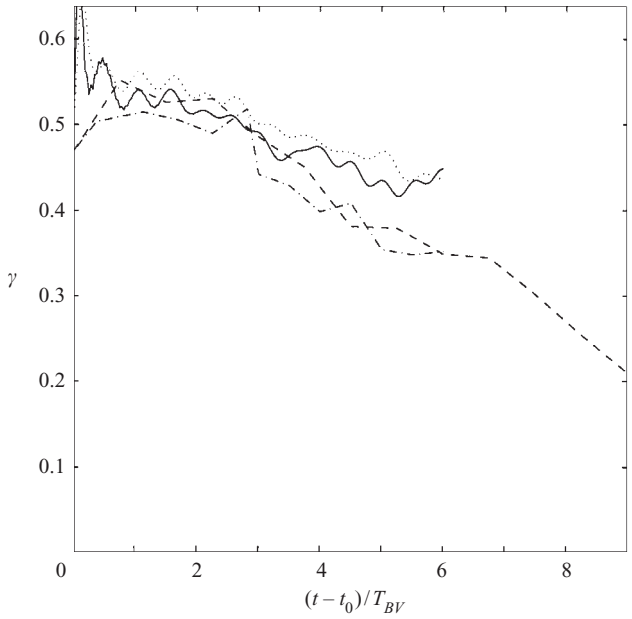

FIGURE 16. Time evolution of the mixing efficiency γ. DNS results for: ——, run R2; ···, run R1; – – – –, run A; —·—·—, run B.

Figure 15 shows that the Cox number reaches a very small value at one Brunt–Väisälä period, when vertical diffusivity becomes close to molecular diffusivity, differing by less than 10%. Hence, the flow is only weakly turbulent from this time on but, K_d being an integrated value, local turbulent mixing may still occur intermittently.

7.2. *Mixing efficiency*

The efficiency with which mixing occurs is quantified by the amount of potential energy (per unit time, for instance) resulting from turbulent mixing processes divided by the amount of energy (per unit time as well) brought to the fluid. In the absence of external forcing, the dissipation rate of kinetic energy is used in place of the input rate of energy. The mixing efficiency is then defined as

$$\gamma = \frac{\chi/N^2}{\epsilon}. \tag{7.3}$$

The mixing efficiency is often quantified by a flux Richardson number $R_f = \gamma/(1+\gamma)$ in place of γ.

DNS results for runs R1 and R2 are compared to those for the lowest-diffusivity runs A and B in figure 16. (Note that diffusivity, not viscosity, matters in the study of mixing.) Two regimes should be distinguished. Up to $\sim 2.8T_{BV}$, the four curves behave identically, except for the very beginning of the runs, with γ staying close to 0.55. Note that an intermediate regime may also be distinguished for runs R1 and R2: γ remains constant up to $1.5T_{BV}$, then starts to decrease slowly. The high value of γ indicates that the flow is turbulent with widespread overturnings. The same constant value of 0.55 is found in DNS of a strongly stably stratified shear layer when three-dimensional small-scale secondary instabilities develop (Staquet 2000). A diffusivity-dependent behaviour can be observed for γ from $t \sim 2.8T_{BV}$: in runs R1

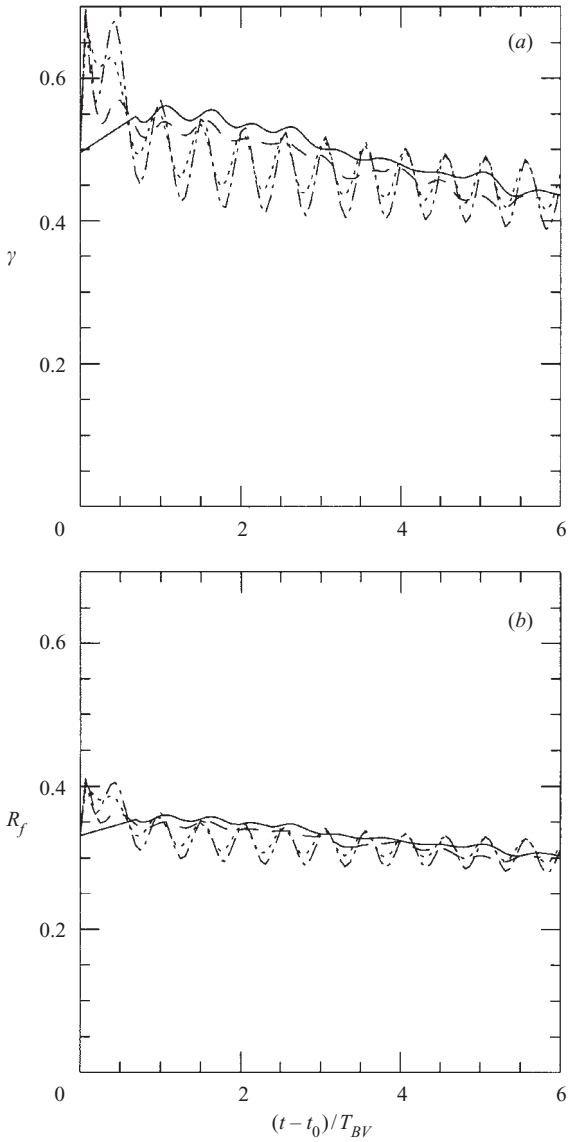

FIGURE 17. Time evolution of: (*a*) the mixing efficiency γ; (*b*) the flux Richardson number R_f. DNS results for run R2 (———), and for run R1 (– – – –). EDQNM results for run R2 (· · ·), and for run R1 (— — — —).

and R2, γ remains at a high level, though slowly decaying, and reaches 0.45 at $6T_{BV}$. In the lowest-viscosity runs A and B by contrast, γ continuously decreases, down to $\sim$0.2 at $9T_{BV}$. The re-laminarization process that occurs at small scales accounts for this behaviour. We have checked that ϵ has very similar values for runs A and R2 on the one hand, and B and R1 on the other hand while, as seen on figure 12, χ/N^2 is lower when ν is lower, at given N. The interpretation of runs R1 and R2 is clear: molecular diffusion makes a strong contribution to mixing, thus masking the re-laminarization process and this results in the high value for γ.

The mixing efficiency and flux Richardson number are plotted in figure 17 for runs R1 and R2, in order to compare the EDQNM$_2$ predictions with the DNS

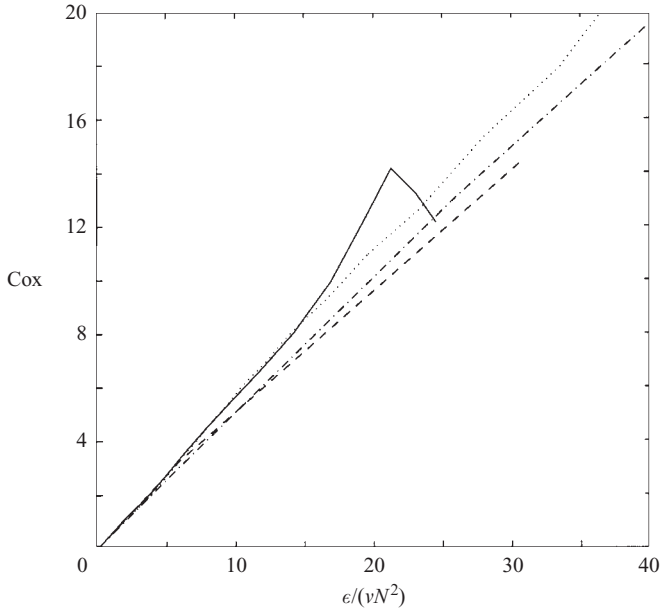

FIGURE 18. Cox number versus $\epsilon/\nu N^2$ for DNS results. ——, run R2; ···, run R1; – – – –, run A; — · — · —, run B.

results. The EDQNM$_2$ model under-estimates by at most 15% the mean value of γ found by DNS (except at the beginning of the computations). These predictions become quite satisfactory from 3 Brunt–Väisälä periods. When the bounded quantity R_f is considered, the EDQNM$_2$ predictions agree with those of the DNS from the beginning of the runs.

In § 6, we have shown that, from $(t - t_0)/T_{BV} \simeq 2$, the dissipation rate of kinetic energy ϵ is approximated well by its axisymmetric expression using two gradients only, $\tilde{\epsilon}_A$. We also found that, from $(t - t_0)/T_{BV} \simeq 2$, the dissipation rate of half the fluctuating temperature variance χ is approximated well by (6.14). It follows that a simple expression for the mixing efficiency can be proposed, which is based upon three gradients only:

$$\gamma = (2\alpha + 1)\frac{\kappa}{N^2}\frac{\overline{(\partial T/\partial z)^2}}{\tilde{\epsilon}_A}. \tag{7.4}$$

Finally, it is useful at this stage to investigate how the Cox number varies as a function of $\epsilon/\nu N^2$, which is a measure of turbulence intensity (e.g. Lienhard & Van Atta 1990; Barry *et al.* 2001). Results are plotted for runs R1, R2, A and B in figure 18. The four curves collapse remarkably well on a single curve of Cox $= 0.5\,\epsilon/\nu N^2$. This dependence can be easily accounted for once γ is known, since $\mathrm{Cox}/(\epsilon/\nu N^2) = Pr\,(\chi/N^2)/\epsilon = Pr\,\gamma$; the values $Pr = 1$ and $\gamma \simeq 0.5$ yield the observed law for the Cox number. Such a linear dependence matches the experimental finding of Barry *et al.* (2001) for $\epsilon/\nu N^2$ smaller than 300, and the results of Bouruet-Aubertot *et al.* (2001) for breaking gravity waves of small amplitude.

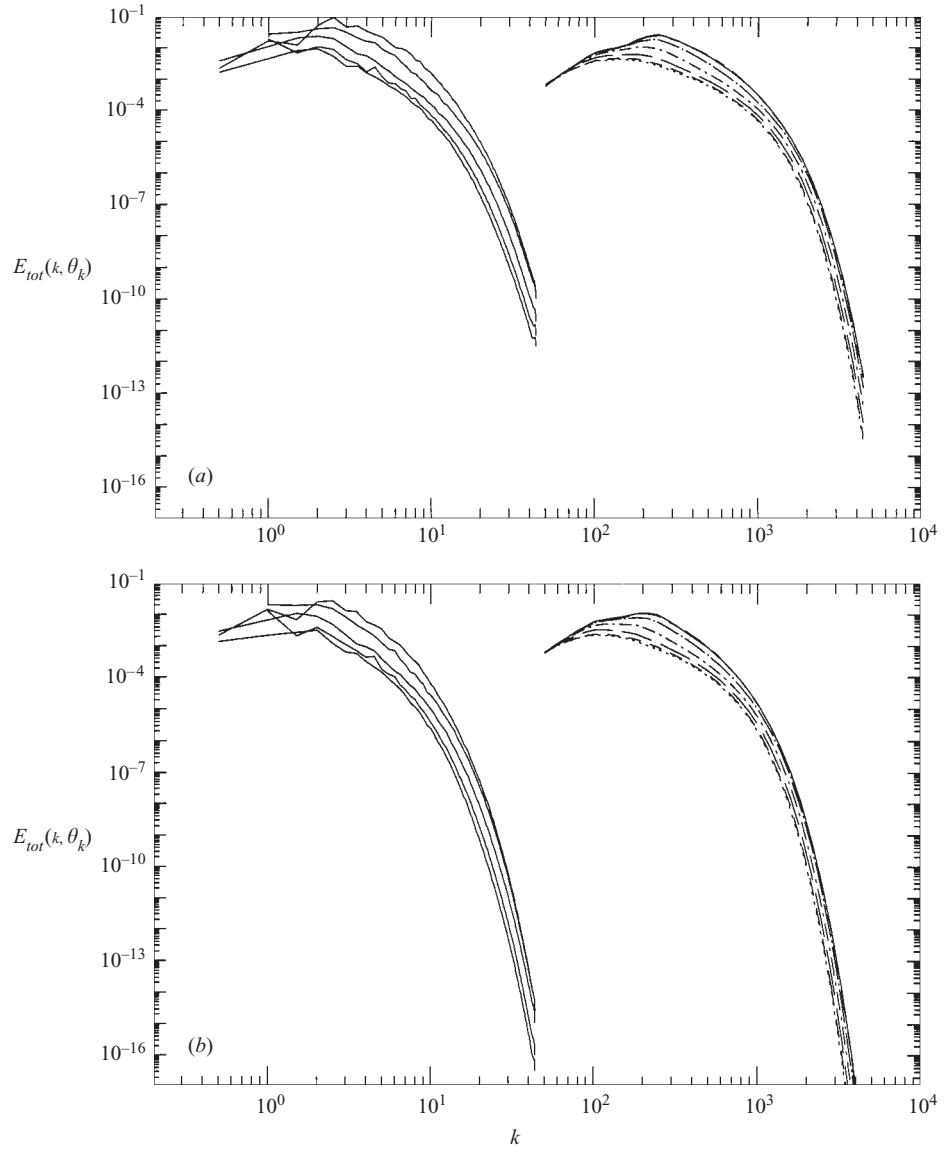

FIGURE 19. Anisotropic total energy spectra at $t - t_0 = 6T_{BV}$: (*a*) run R2; (*b*) run R1. Spectra on the left are DNS data, while the spectra on the right are $EDQNM_2$ data, shifted two decades to the right. The more energetic spectra (top curves) correspond to wavevectors close to the *polar* direction, and the bottom spectra for the *equatorial* orientation of wavevectors. There are a total of five orientations in between for DNS, and seven for $EDQNM_2$.

8. Spectra

8.1. *Directivity*

Figures 19 and 20 show the dependence of the energy spectra upon θ_k. DNS spectra are computed from equation (3.1). The DNS discretization accounts for the lack of sampling at the smallest wavevectors for some orientations, where no grid point lies within the integration domain. The statistical model is free of this problem, since

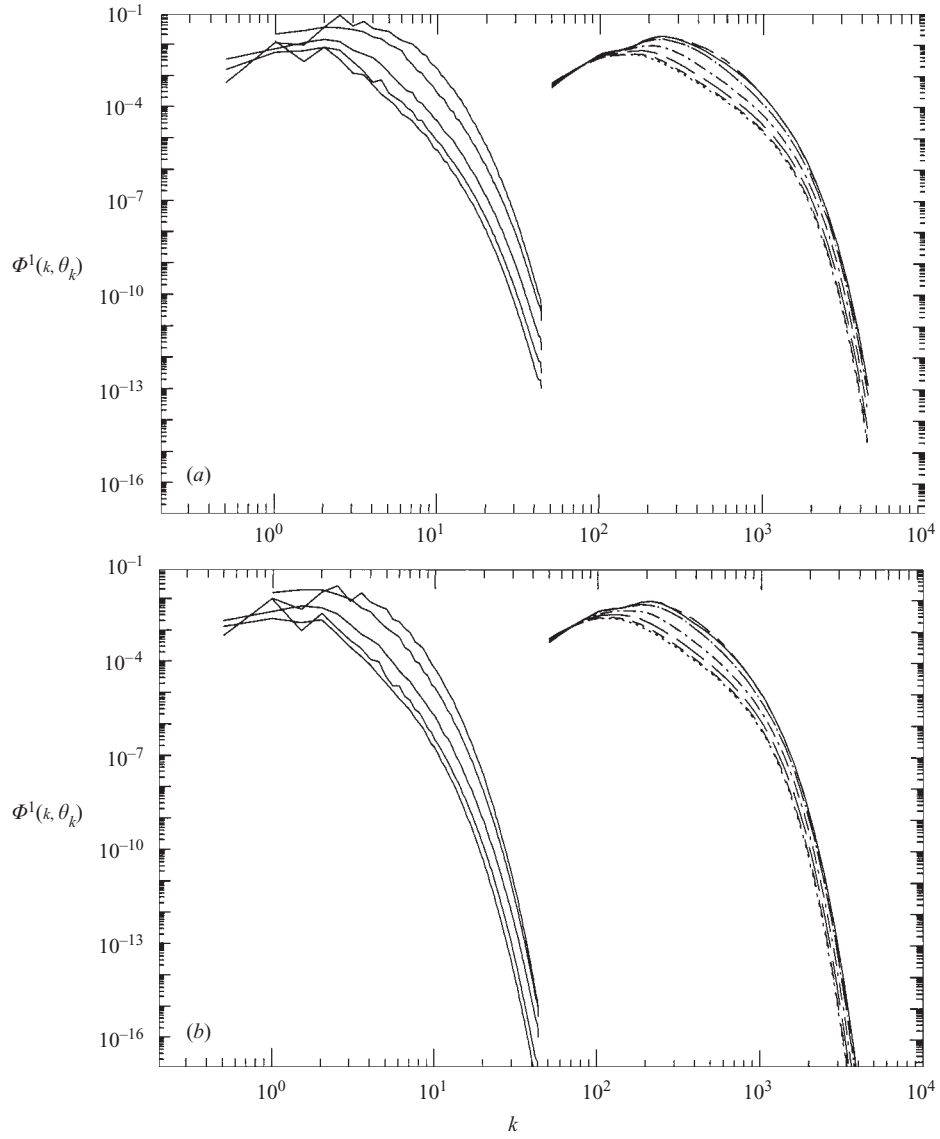

FIGURE 20. Anisotropic vortex energy spectra at $t - t_0 = 6T_{BV}$: (*a*) run R2; (*b*) run R1. For details refer to the caption of figure 19.

it gives direct access to angular-dependent energy density spectra, shown on the same figures, on mesh points adapted to the spectral energy distribution (that is, the discretization is refined towards small wavevectors).

In isotropic homogeneous turbulence, spectra at all θ_k coincide. By contrast, in the present stratified flow, only the largest scales, that feed the turbulent cascade, are mainly isotropic (figures 19 and 20). The largest anisotropy is in the intermediate subrange for both the vortex and the wave mode spectra. Also, the smaller θ_k, the more energetic the spectrum. Hence, as expected, energy concentrates in horizontal motion, with the exhibited θ_k-distribution.

The figures also show that energy levels are higher for $N = \pi$ than for $N = \pi/2$ at all wavenumbers and for all angles, due to the stronger inhibition of energy transfers in the former case than in the latter. This remark holds for both the total energy spectra and the vortex kinetic energy spectra. It was shown in Part 1 that the overall prediction for the level of the θ_k-integrated spectra by the $EDQNM_2$ model matches DNS results. The present analysis permits one to refine this result: directional anisotropy is qualitatively reproduced well by the model, the agreement being even quantitative for run R1 (figure 19). In run R2 (figure 20) DNS shows significantly larger directional anisotropy, a trend not reproduced by $EDQNM_2$. For this last run, the kinetic energy spectrum is strongly dependent on the orientation of the wavevector, down to the smallest scales in the flow, thereby constituting evidence of strong anisotropy in the dissipative range, with a two-decade gap between the polar and the equatorial spectra. The vortex kinetic energy spectrum itself is only slightly less anisotropic in the smallest scales. The $EDQNM_2$ model predicts some directional dependence of the dissipative range of the spectra, but it seems to be due to local transfers only. Anisotropy transferred by non-local triadic interactions, down to the smallest dissipative range, probably needs improved modelling in $EDQNM_2$. In this respect, the work by Yeung, Brasseur & Wang (1995) may shed light, for they have proposed an extensive analysis, relating both spectral and physical space, of the long-range triadic interactions and their role on the isotropization of the small scales.

8.2. *Remark on polarization anisotropy of the spectra*

Polarization anisotropy refers to the possible difference between $\hat{\phi}^1$ and $\hat{\phi}^2$ at given $\boldsymbol{k}$, thus indicating predominance of either the vortex or wave components of the velocity. Polarization anisotropy becomes of much less importance when directional anisotropy is strong, such that energy accumulates in vertical wavevectors, since axisymmetry imposes $\Phi_1 = \Phi_2$. At long times or for very small Froude numbers, polarization will be negligible. On the other hand, for turbulence subjected to solid-body rotation, Cambon *et al.* (1997) have shown that energy accumulates at horizontal wavevectors, where no such axisymmetry constraint holds. In that case quantifying polarization is important for describing the columnar structuring of the flow. In the stratified case, a detailed description of polarisation anisotropy may eventually be of importance for the improved modelling of the initial stages of decay of stably stratified turbulence.

9. Discussion and conclusion

We have investigated stably stratified freely decaying turbulence, both from the point of view of direct numerical simulations and that of two-point statistical modelling. Following the first part of this work reported in Part 1, regarding the evolution of energetics, we have focused in the present work on investigating the detailed anisotropy appearing in the flow.

Our simulations have been performed using large initial potential energy conditions, at variance with grid-turbulence laboratory experiments. This initial condition, designed to validate the statistical model, appears to yield results comparable to those stemming from DNS with zero initial potential energy (and to laboratory experiments as well). Large-scale anisotropy was characterized by the ratio of r.m.s. fluctuating velocity components u/w. This indicator saturates at a value close to 1.5, in agreement with experimental values. The corresponding flow is therefore twice as energetic in the horizontal directions as in the vertical one. Information on the structure of the flow is

provided by transverse and longitudinal correlation length scales. These length scales show that the flow is organized into layers that are vertically decorrelated, resulting in the well-known 'pancake-shaped' large-scale vortices. Indeed, the action of stable stratification inhibits almost completely the growth of the vertical length scales, as expected, while horizontal length scales continue to grow. The growth rate of the latter scales is close to the isotropic three-dimensional growth rate and, therefore, to the two-dimensional rate as well so that no conclusion about the flow dynamics can be inferred from this scale behaviour. By contrast, simple scaling arguments show that the vertical scale is set by the shear induced by the quasi-horizontal vortices and by buoyancy. We checked that the Froude number thus defined indeed remains of order one throughout the flow evolution, from the time the smallest scales feel buoyancy. This result matches the theoretical predictions of Billant & Chomaz (2001) for an inviscid fluid.

These processes accompany the concentration of energy towards vertical wavevectors in the two-point statistical spectra, demonstrating the duality between the physical space concept of 'collapse-layering' and the spectral space one, of 'directional dependence'. We also note that vertical correlation lengths of vertical velocity components oscillate with large amplitudes, an indication of the strong dynamical response of the flow under the action of internal gravity waves.

The predictions of the statistical model for large-scale anisotropy are in agreement with DNS results, starting from the u/w ratio, where the difference with DNS is small, up to its perfect ability to predict the damping of the vertical length scales while retaining the growth of the horizontal one. The only trifling defect, expected from our previous work on the heat flux though, lies in too large an amplitude of oscillation predicted by EDQNM_2, a feature that we also find here in the vertical correlation length for the vertical velocity component. Improvement has to be sought in a modified treatment for the phase of the oscillating quantity $\Phi_2 - \Phi_3 + I\Psi_R$ (see (2.14)).

The small-scale anisotropy has been characterized in physical space through a detailed examination of the velocity gradients. The statistical model predictions are in good agreement with DNS results, in all stages of the decay, from the initially highly turbulent to the final weak turbulent stage. The velocity gradients generate kinetic energy dissipation rate and we have compared several approximations for the dissipation rate of kinetic energy. We found that an isotropic formulation is not valid in our simulations, implying that knowledge of one of the velocity gradients in the flow does not allow one to access the dissipation rate through an isotropic approximation. The use of vertical gradients of the horizontal velocity component leads to an over-estimation of the dissipation, while horizontal gradients of this same component under-estimate it. As long as the axisymmetry of the flow is satisfied, a combination of these two gradients is enough to obtain a better model for dissipation.

With the help of the accurate characterization of small-scale anisotropy in the computed stably stratified turbulence, we have analysed the mixing properties of the flow. The mixing efficiency remains of order 0.5 for two Brunt–Väisälä periods or so and the subsequent behaviour depends on the diffusivity: if it is too high, the diffusivity provides a strong contribution to the mixing efficiency, which remains close to the 0.5 value; if small, mixing becomes controlled by the major process at small scales, which is re-laminarization. The mixing efficiency steadily decreases in this case. Using three gradients of temperature and velocity only, we propose a simple expression for mixing efficiency, which may be useful for experimentalists. In agreement with laboratory experiments, we find that the Cox number displays a

unique dependence after 0.6 Brunt–Väisälä period, when plotted as a function of time normalized by this period, and behaves linearly with the parameter $\epsilon/\nu N^2$.

Regarding spectra of two-point velocity component correlations, good qualitative agreement between EDQNM$_2$ predictions and DNS results is obtained when angular-dependent spectra are considered. These spectra have been shown to contain two types of anisotropy, namely a *directional* dependence upon the orientation of the wavevector to the vertical, and a *polarization* anisotropy that accounts for a difference between the two Craya–Herring modes, that in turn translates, in stably stratified turbulence, into different energy levels between the horizontal vortex motion and the wave motion. The directivity of the spectra is very weak in the most energetic scales, the largest ones, whereas it is largest in the intermediate subrange (though not as large as in DNS), and decreasing in the viscous subrange. However, a noticeable directional anisotropy is still present in the dissipative scales, down to the smallest. Consequently, we expect that predictions from large-eddy simulations of stably stratified turbulence should be improved by means of a non-isotropic formulation of the subgrid-scale models. To our knowledge, spectral models for eddy viscosity are usually based on estimates of the dissipation proportional to $\sqrt{E(k_c)/k_c}$ (though more refined models have been proposed, see Lesieur & Metais 1996 for a review). Looking at the spectra presented in § 8.1, it is clear that angular-dependent spectra should be employed in the estimation of the dissipation at corresponding angles. Moreover, polarization anisotropy (§ 8.2), should be reflected by separate estimates for the vortex and wave modes when their spectra behave differently at the small scales. Such considerations can be important in predicting the dynamics of the atmospheric boundary layer for instance by large-eddy simulations.

This work benefited from computer time allocated by IDRIS run by the French CNRS. We also wish to thank Claude Cambon for many enlightening remarks and Olivier Praud for useful discussions.

Appendix A. Spectral formalism in the frame of linear eigenmodes

A.1. *Craya–Herring local frame of reference*

Note first that the following decomposition of the velocity field presented in physical space is slightly different from that in Part 1, in that it matches more closely the Fourier space decomposition (see e.g. Cambon 2001 for comparison of various such decompositions, including the poloidal/toroidal one by Thual 1992). For completeness, we also introduce a horizontal mean flow in both physical and spectral space decompositions, which was omitted in Part 1.

Let $\boldsymbol{n}$ represent the vertical upward unit vector, $\nabla_h = (\partial/\partial x, \partial/\partial y, 0)$ the gradient operator in the horizontal plane and $\boldsymbol{k}_h = (k_1, k_2)$ the projection of the wavevector onto the horizontal plane. The velocity field can be split as, respectively in physical and spectral space,

$$\left.\begin{aligned} \boldsymbol{u} &= \nabla \times \psi\ \boldsymbol{n} + \nabla \times \nabla \times \xi\ \boldsymbol{n} + \boldsymbol{U}_{\mathrm{m}}(z), \\ \hat{\boldsymbol{u}} &= \hat{\phi}^1\ \boldsymbol{e}^1 + \hat{\phi}^2\ \boldsymbol{e}^2 + \hat{\boldsymbol{U}}(\boldsymbol{k}_h = 0, k_3 \neq 0). \end{aligned}\right\} \tag{A 1}$$

In physical space, two scalar functions are introduced, namely ψ and ξ. The first term can be identified as the horizontal motion associated with the vertical vorticity in the flow. The second term contains the vertical velocity of the flow. The third term is a horizontal mean flow, which may have a vertical variability. In stably stratified homogeneous turbulence, this mean flow results from the internal gravity wave field,

either from the finite amplitude of the wave field – much like the Stokes drift for surface waves – or from dissipative effects associated with the waves (e.g. McIntyre & Norton 1990). Here the waves are generated by a turbulent field with randomly distributed wavevectors, so that the resulting mean flow should locally vanish or, at least, be of weak energy content compared to the total kinetic energy of the flow. This property is expressed in the axisymmetry, i.e. the statistical isotropy about the vertical axis assumed in – and inherent to – the statistical EDQNM$_2$ model. It should be noted that, in a direct numerical simulation, a mean flow may result from geometrical confinement: if energy is injected at a scale close to the domain size, inverse transfers of energy toward scales larger than the domain size will yield a horizontal mean flow. As discussed in the first part of this work, the domain size has been chosen large enough, with respect to the scale at which energy is injected, so that the storage of energy resulting from this confinement effect remains insignificant for the 6 Brunt–Väisälä periods over which the flow analysis is conducted.

It is important to stress that decomposition (A 1) is a mathematical one. It relates exactly to separately identified physical items (namely waves and a horizontal vortex), in the limit of zero Froude number only (that is, when the nonlinear time scale is infinitely small relative to N^{-1}), although the corresponding physical meaning is still of great interest in the fully nonlinear context. In the very small Froude number limit, the first term of the decomposition becomes a good approximation of the non-propagating vortex part (also referred to as the vortical part, in the literature) and the second term represents the velocity field of the internal waves. When this limit is not reached, the first two terms of the decomposition are normally contributed by a wave *and* a vortex part. Again, we shall see that the decomposition can actually be given a physical meaning even if this limit is not reached, as soon as the Froude number becomes smaller than one.

Equivalently, in spectral space, the decomposition becomes a geometrical one, and the fluctuating velocity vector is split into three modes, which we denote $\hat{\boldsymbol{\phi}}^1(\boldsymbol{k}, t)$, $\hat{\boldsymbol{\phi}}^2(\boldsymbol{k}, t)$ and $\hat{U}(\boldsymbol{k}_h = 0, k_z \neq 0)$. The first two modes are obtained by using the components of the spectral fluctuating velocity in the Craya–Herring frame (Craya 1958; Herring 1974), which is local to the wavevector $\boldsymbol{k}$. The corresponding unit vectors are

$$\boldsymbol{e}^1(\boldsymbol{k}) = (\boldsymbol{k} \times \boldsymbol{n})/|\boldsymbol{k} \times \boldsymbol{n}|\,, \quad \boldsymbol{e}^2(\boldsymbol{k}) = (\boldsymbol{k} \times \boldsymbol{e}^1)/|\boldsymbol{k} \times \boldsymbol{e}^1|\,, \quad \boldsymbol{e}^3(\boldsymbol{k}) = \boldsymbol{k}/|\boldsymbol{k}|. \tag{A 2}$$

The first one supports the non-propagating vortex mode of velocity fluctuations, and the second one accounts for the wave part. Note that these vectors are not defined when $\boldsymbol{k}$ is parallel to $\boldsymbol{n}$, the associated motion being accounted for by the horizontal mean flow. It is straightforward to show that the $\hat{\boldsymbol{\phi}}^1$ and $\hat{\boldsymbol{\phi}}^2$ components are related to Fourier transforms of the scalar functions ψ and ξ by $\hat{\boldsymbol{\phi}}^1 = \boldsymbol{I}\ |\boldsymbol{k}_h|\ \hat{\psi}$ and $\hat{\boldsymbol{\phi}}^2 = -|\boldsymbol{k}|\ |\boldsymbol{k}_h|\ \hat{\xi}$.

Because of statistical isotropy around the vertical axis implicitly assumed in this description, two-point statistics for $\hat{\boldsymbol{\phi}}^1$ and $\hat{\boldsymbol{\phi}}^2$ do not depend upon the azimuthal angle of $\boldsymbol{k}$.

A.2. *Formulation using the total energy variable*

As a way of simplifying the algebra of the four-dimensional system of Boussinesq equations, we have reduced the system in spectral space to a three-dimensional one by using the divergenceless property of the velocity field. The algebra can be further unified by re-writing the system of equations in terms of a vector variable $\hat{\boldsymbol{v}}$ that

combines the fluctuating velocity components and the temperature; $\hat{\boldsymbol{v}}$ is such that its density spectrum gives the total energy in the flow, as the sum of the kinetic and potential energies:

$$\hat{v}_i^* \hat{v}_i/2 = \hat{u}_i^* \hat{u}_i/2 + \hat{T}^* \hat{T}/(2N^2)$$

(Cambon 1989; Godeferd & Cambon 1994), by means of a dynamical scaling of temperature by the factor $\beta g/N$. The new vector variable is therefore

$$\hat{\boldsymbol{v}}(\boldsymbol{k}, t) = \hat{\phi}^1(\boldsymbol{k}, t)\boldsymbol{e}^1(\boldsymbol{k}) + \hat{\phi}^2(\boldsymbol{k}, t)\boldsymbol{e}^2(\boldsymbol{k}) + \hat{U}(\mathbf{k}_h = 0, k_3 \neq 0) + \hat{\phi}^3(\boldsymbol{k}, t)\boldsymbol{e}^3(\boldsymbol{k}), \qquad \text{(A 3)}$$

where $\hat{\phi}^3 = (I/N)\hat{T}$. The equation for $\hat{\boldsymbol{v}}$ simply becomes

$$\left[\frac{\partial}{\partial t} + \nu k^2\right] \hat{\boldsymbol{v}}(\boldsymbol{k}, t) + \boldsymbol{L}(\boldsymbol{k})\hat{\boldsymbol{v}}(\boldsymbol{k}, t) = \int_{\boldsymbol{k}+\boldsymbol{p}+\boldsymbol{q}=\boldsymbol{0}} (\boldsymbol{M}(\boldsymbol{k}, \boldsymbol{p}, \boldsymbol{q})\hat{\boldsymbol{v}}(\boldsymbol{q}, t))\, \hat{\boldsymbol{v}}(\boldsymbol{p}, t)\, \mathrm{d}^3\boldsymbol{p}, \qquad \text{(A 4)}$$

where the linear operator $\boldsymbol{L}$ contains the explicit effect of stratification, as a coupling between the components of $\hat{\boldsymbol{v}}$, and the right-hand side accounts for the nonlinear interaction with coefficients in the third-order tensor $\boldsymbol{M}$, such that

$$\left.\begin{aligned} L_{ij}(\boldsymbol{k}) &= IN\left[P_{i3}(\boldsymbol{k})\frac{k_j}{k} + P_{j3}(\boldsymbol{k})\frac{k_i}{k}\right], \\ M_{ipq}(\boldsymbol{k}, \boldsymbol{p}, \boldsymbol{q}) &= -Ik_l P_{lp}(\boldsymbol{p})\left[P_{in}(\boldsymbol{k})P_{nq}(\boldsymbol{q}) + \frac{k_i q_q}{kq}\right]. \end{aligned}\right\} \qquad \text{(A 5)}$$

It is important to stress that equation (A 4) has the same shape as the classical spectral Navier–Stokes equations for isotropic turbulence, so that the procedure of constructing a statistical two-point model can be formally performed in the same way, starting from (A 4), as for the classical isotropic case (see Part 1). Of course, in the following, when deriving the EDQNM$_2$ model, we must bear in mind that one of the components of $\hat{\boldsymbol{v}}$ is related to temperature and not velocity, so that the phenomenological arguments for the closure should be different.

Appendix B. The EDQNM$_2$ model for stratified turbulence

As previously mentioned, equation (2.11) is an unclosed equation. Indeed, the energy transfer terms $\boldsymbol{T}$, that redistribute energy among wavevector space, and allow for net energy exchange between wave kinetic, vortex kinetic and potential energies, are expressed in terms of the fourth-order correlation spectra. These are usually modelled as a function of the components of $\boldsymbol{Q}$ through a quasi-Gaussian hypothesis, allowing one to transform (2.11) into an implicitly closed equation for the components of $\boldsymbol{Q}$. Several two-point statistical models have been used for solving the closure problem and the EDQNM model, useful for its tractability, will be considered here. This model has been developed by several authors in the past for isotropic turbulence (see e.g. Orszag 1970). It is still the object of active development within an anisotropic context. In the case of rotating (Cambon *et al.* 1997) as well as stratified flows, the specificity of this so-called EDQNM$_2$ model relies on its including the linear operator in the triple correlations of velocity. We shall not describe again the general principles of EDQNM modelling, nor the way it has been extended to the stably stratified case to take into account the dynamics of internal gravity wave field, and its interaction with the turbulent field. The reader can refer to Part 1 for a list of references and a discussion of the merits of various two-dimensional and three-dimensional modelling endeavours.

We only focus here on two specific features of the anisotropic EDQNM model. First, in the linear limit, the model provides exact solutions to the linearized Navier–Stokes equations, and the triadic interaction timescale – to take into account the wave or vortex nature of each of the modes in the triad – appears naturally in our formulation, as a modification of the isotropic one

$$\tau_{kpq} = \nu(k^2 + p^2 + q^2) + \mu(k) + \mu(p) + \mu(q) \tag{B 1}$$

to account for the dispersion relation of the waves ($\mu(k)$ is defined by equation (B 3) below).

We use the Green's function solution as an alternative way of writing the unsolved system of equations, so that the linear operator $\boldsymbol{\Lambda}$ is implicitly solved. By this procedure, the modelled nonlinear transfer term in equation (2.11), as an integral over all possible triadic energy transfers, accounts directly for the time scale $1/\omega^{\varepsilon}$ of each mode of the triad involved (the ε can be one of 0, -1, 1). The frequencies are $\omega_k^{\pm 1} = \pm N \sin\theta_k$ for a wave mode of wavevector $\boldsymbol{k}$, and $\omega_k^0 = 0$ for a vortex one. Hence, τ_{kpq} is replaced, in the anisotropic model, by

$$\tau_{kpq}^{\varepsilon\varepsilon'\varepsilon''} = \left[\tau_{kpq}^{-1} - IN(\varepsilon \sin\theta_k + \varepsilon' \sin\theta_p + \varepsilon'' \sin\theta_q)\right]^{-1}. \tag{B 2}$$

Note that the latter sum of three pulsations, when zero, removes all explicit effect of N in the nonlinear time scale, a condition which is known as 'resonance'. The resonance condition is naturally satisfied for interactions between three vortex modes. Therefore, when N becomes very large, only off-resonant triads (necessarily among wave modes) act over a much smaller time scale. It follows that, in the EDQNM$_2$ model, energy transfers are controlled either by vortex modes or by resonant triads among waves (possibly involving one vortex mode, see Lelong & Riley 1991).

This triadic time scale arises naturally from the eigenmodes of the corresponding linear system of equations, with no extra assumption other than that of the original isotropic model. Thus this method is general enough to be applicable to a wide range of external body forces, that come into play in the Navier–Stokes equations through a linear term.

A second important parameter of the EDQNM model is an *ad hoc* inverse time scale

$$\mu(k) = 0.366 \int_0^k p^2 E(p)\,\mathrm{d}p \tag{B 3}$$

introduced for taking into account the departure of the actual velocity distribution from an exact Gaussian one. The multiplicative constant in (B 3) comes from the tuning of the isotropic EDQNM model for recovering the Kolmogorov constant, but has remained unchanged ever since the first time it was set (André & Lesieur 1977). Herring & Kraichnan (1971) and Orszag (1970) showed that $1/\mu(k)$ can be interpreted as a decorrelation time scale of a vortex structure of size k. The crux in anisotropic EDQNM$_2$ modelling is to choose this decorrelation time scale wisely. In the present model, we have decided to keep the definition of μ unchanged with respect to the isotropic model, though the physical argument underlying (B 3) is not directly applicable to internal waves or to the scalar (temperature) field. We have nevertheless demonstrated that this straightforward way provides an EDQNM$_2$ model for stably

stratified turbulence which agrees very well with DNS computations (reported in Part 1).

REFERENCES

André, J. C. & Lesieur, M. 1977 Influence of helicity on high Reynolds number isotropic turbulence. *J. Fluid Mech.* **81**, 187–207.

Barry, M. E., Ivey, G. N., Winters, K. B. & Imberger, J. 2001 Measurements of diapycnal diffusivities in stratified fluids. *J. Fluid Mech.* **442**, 267–291.

Batchelor, G. K. 1946 The theory of axisymmetric turbulence. *Proc. R. Soc. Lond.* A **186**, 480–502.

Batchelor, G. K. 1953 *The Theory of Homogeneous Turbulence*. Cambridge University Press.

Billant, P. & Chomaz, J.-M. 2001 Self-similarity of strongly stratified inviscid flows. *Phys. Fluid* **13**, 1645–1651.

Bouruet-Aubertot, P., Koudella, C., Staquet, C. & Winters, K. B. 2001 Particle dispersion and mixing by breaking internal gravity waves: two-dimensional numerical experiments. *Dyn. Atmos. Oceans* **33**, 95–134.

Boussinesq, J. 1901 *Théorie Analytique de la Chaleur*. Gauthier-Villars, Paris.

Bryan, F. 1987 Parameter sensitivity of primitive equation ocean general circulation models. *J. Phys. Oceanogr.* **17**, 970–985.

Caillol, P. & Zeitlin, V. 2000 Kinetic equations and stationary energy spectra of weakly nonlinear internal gravity waves. *Dyn. Atmos. Oceans* **32**, 81–112.

Cambon, C. 1989 Spectral Approach to Axisymmetric Turbulence in a Stratified Fluid. *Advances in Turbulence* 2 (ed. H.-H. Fernholz & H. E. Fiedler). Springer.

Cambon, C. 2001 Turbulence and vortex structures in rotating and stratified flows. *Eur. J. Mech.* B *Fluids* **20**, 489–510.

Cambon, C., Mansour, N. N. & Godeferd, F. S. 1997 Energy transfer in rotating turbulence. *J. Fluid Mech.* **337**, 303–332.

Canuto, C., Hussaini, M. Y., Quarteroni, A. & Zang, T. A. 1988 *Spectral Methods in Fluid Dynamics*. Springer.

Craya, A. D. 1958 Contribution à l'analyse de la turbulence associée à des vitesses moyennes. PST 345. Ministère de l'Air, France.

Fincham, A. M., Maxworthy, T. & Spedding, G. R. 1996 Energy dissipation and vortex structure in freely-decaying stratified grid-turbulence. *Dyn. Atmos. Oceans* **23**, 155–169.

Gargett, A. E., Osborn, T. R. & Nasmyth, P. W. 1984 Local isotropy and the decay of turbulence in a stratified fluid. *J. Fluid Mech.* **144**, 231–280.

Godeferd, F. S. & Cambon, C. 1994 Detailed investigation of energy transfers in homogeneous stratified turbulence. *Phys. Fluids* **6**, 2084–2100.

Hanazaki, H. & Hunt, J. C. R. 1996 Linear processes in unsteady stably stratified turbulence. *J. Fluid Mech.* **318**, 303–337.

vanHaren, L., Staquet, C. & Cambon, C. 1996 Decaying stratified turbulence: comparison between a two-point closure EDQNM model and direct numerical simulations. *Dyn. Atmos. Oceans* **23**, 217–245.

Herring, J. R. 1974 Approach of axisymmetric turbulence to isotropy. *Phys. Fluids* **17**, 859–872.

Herring, J. R. & Kraichnan, R. H. 1971 Comparison of some approximations for isotropic turbulence. In *Statistical Models and Turbulence*, Lecture Notes in Physics, vol. 12 (ed. J. Ehlers, K. Hepp & H. A. Weidenmller). Springer.

Herring, J. R. & Metais, O. 1989 Numerical experiments in forced stably stratified turbulence. *J. Fluid Mech.* **202**, 97–115.

Holliday, D. & McIntyre, M. E. 1981 On potential energy density in an incompressible stratified fluid. *J. Fluid Mech.* **107**, 221–225.

Huq, P. & Stretch, D. D. 1995 Critical dissipation rates in density stratified turbulence. *Phys. Fluids* **7**, 1034–1039.

Itsweire, E. C., Helland, K. N. & Van Atta, C. W. 1986 The evolution of grid-generated tubulence in a stably stratified fluid. *J. Fluid Mech.* **162**, 299–338.

Lelong, M. P. & Riley, J. J. 1991 Internal wave-vortical mode interactions in strongly stratified flows. *J. Fluid Mech.* **232**, 119.

Lesieur, M. 1990 *Turbulence in Fluids*, 2nd Edn. Kluwer.

Lesieur, M. & Metais, O. 1996 New trends in large-eddy simulations of turbulence. *Annu. Rev. Fluid Mech.* **28**, 45–82.

Lienhard, J. H. & Van Atta, C. W. 1990 The decay of turbulence in thermally stratified flow. *J. Fluid Mech.* **210**, 57–112.

Lilly, D. K. 1983 Stratified turbulence and the mesoscale variability of the atmosphere. *J. Atmos. Sci.* **40**, 749–761.

Lin, J.-T. & Pao, Y.-H. 1979 Wakes in stratified fluids. *Annu. Rev. Fluid Mech.* **11**, 317–338.

Lorenz, E. 1955 Available potential energy and the maintenance of the general circulation. *Tellus* **7**, 157–167.

McIntyre, M. E. & Norton, W. A. 1990 Dissipative wave-mean interactions and the transports of vorticity or potential vorticity. *J. Fluid Mech.* **212**, 403–435; and Corrigendum **220**, 693.

Metais, O. & Herring, J. R. 1989 Numerical simulations of freely evolving turbulence in stably stratified fluids. *J. Fluid Mech.* **202**, 117–148.

Orszag, S. A. 1970 Analytical theories of turbulence. *J. Fluid Mech.* **41**, 363.

Osborn, T. R. & Cox, C. S. 1972 Oceanic fine structure. *Geophys. Fluid Dyn.* **3**, 321–345.

Piccirillo, P. & Van Atta, C. W. 1997 The evolution of uniformly sheared thermally stratified turbulent flow. *J. Fluid Mech.* **334**, 61–86.

Ramsden, D. & Holloway, G. 1992 Energy transfers across an internal wave-vortical mode spectrum. *J. Geophys. Res.* **97**, 3659–3668.

Reynolds, W. C. & Kassinos, S. 1995 One-point modelling of rapidly deformed homogeneous turbulence. *Osborne Reynolds Centenary Volume, Proc. R. Soc. Lond.* A 451, 87–104.

Riley, J. J. & Lelong, M.-P. 2000 Fluid motions in the presence of strong stable stratification. *Annu. Rev. Fluid Mech.* **32**, 613–657.

Riley, J. J., Metcalfe, R. W. & Weissman, M. A. 1981 Direct numerical simulations of homogeneous turbulence in density-stratified fluids. In *Proc. AIP Conf. on Nonlinear Properties of Internal Wave* (ed. B. J. West), pp. 79–112. American Institute of Physics.

Rogallo, R. S. 1981 Numerical experiments in homogeneous turbulence. *NASA Tech. Mem.* 81315.

Sidi, C. 1995 Some observed properties of small scale ($o[1..10^2\,m]$) fluctuations in the stratosphere. *Proc. Euromech Colloquium* 339 (ed. C. Staquet).

Siegel, D. A. & Domaradzki, J. A. 1994 Large Eddy Simulation of Decaying Stratified Turbulence. *J. Phys. Oceangr.* **24**, 1353–1386.

Sommeria, J. 2002 Two-dimensional turbulence. *Les Houches, Ecole d'Été de Physique Théorique*, vol. 74. Springer.

Staquet, C. 2000 Mixing in a stably stratified shear layer: two- and three-dimensional numerical experiments. *Fluid Dyn. Res.* **27**, 367–404.

Staquet, C. & Godeferd, F. S. 1998 Statistical modelling and direct numerical simulations of decaying stably stratified turbulence. Part 1. Energetics. *J. Fluid Mech.* **360**, 295–340.

Stillinger, D. C., Helland, K. N. & Van Atta, C. 1983 Experiments on the transition of homogeneous turbulence to internal waves in a stratified fluid. *J. Fluid Mech.* **131**, 91–122.

Thoroddsen, S. T. & Van Atta, C. W. 1992 The influence of stable stratification on small-scale anisotropy and dissipation in turbulence. *J. Geophys. Res.* **97** (C3), 3647–3658.

Thoroddsen, S. T. & Van Atta, C. W. 1996 Experiments on density-gradient anisotropies and scalar dissipation of turbulence in a stably stratified fluid. *J. Fluid Mech.* **322**, 383–409.

Thorpe, S. A. 1977 Turbulence and mixing in a scottish loch. *Phil. Trans. R. Soc. Lond.* **286**, 125–181.

Thual, O. 1992 Zero-Prandtl-number convection. *J. Fluid Mech.* **240**, 229–258.

Toole, J. M. 1998 Turbulent Mixing in the Ocean: Intensity, Causes, and Consequences. In *Ocean Modeling and Parameterization* (ed. E. P. Chassignet & J. Verron) pp. 171–190. Kluwer.

Townsend, A. A. 1976 *The Structure of Turbulent Shear Flow*. Cambridge University Press.

Vincent, A. & Meneguzzi, M. 1991 The spatial structure and statistical properties of homogeneous turbulence. *J. Fluid Mech.* **225**, 1–20.

Winters, K. B., Lombard, P. N., Riley, J. J. & D'Asaro, E. A. 1995 Available potential energy and mixing in stratified fluids. *J. Fluid Mech.* **289**, 115–128.

Yamazaki, H. & Osborn, T. 1990 Dissipation estimates for stratified turbulence. *J. Geophys. Res.* **95**, 9739–9744.

Yamazaki, H. & Osborn, T. 1993*a* Correction to "Dissipation estimates for stratified turbulence". *J. Geophys. Res.* **98**(12), 605.

Yamazaki, H. & Osborn, T. 1993*b* Direct estimation of heat flux in a seasonal thermocline. *J. Phys. Oceanogr.* **23**, 503–516.

Yeung, P. K., Brasseur, J. G. & Wang, Q. 1995 Dynamics of direct large-small scale couplings in coherently forced turbulence: concurrent physical- and Fourier-space views. *J. Fluid Mech.* **283**, 43–95.

Yoon, K. & Warhaft, Z. 1990 The evolution of grid-generated turbulence under conditions of stable thermal stratification. *J. Fluid Mech.* **215**, 601–638.